Received 25 October 2022; revised 28 November 2022; accepted 8 December 2022. Date of publication 19 December 2022; date of current version 4 January 2023.

Digital Object Identifier 10.1109/OJCOMS.2022.3230327

A Unified Framework for Full-Duplex Massive MIMO Cellular Networks With Low Resolution Data Converters

ELYES BALTI (Graduate Student Member, IEEE), AND BRIAN L. EVANS (Fellow, IEEE)

6G@UT Research Center, Wireless Networking and Communications Group, The University of Texas at Austin, Austin, TX 78712 USA

CORRESPONDING AUTHOR: E. BALTI (e-mail: ebalti@utexas.edu)

This work was supported by NVIDIA and AT&T Labs, which are affiliates of the 6G@UT Research Center.

This work is an expanded version of [1], [2], [3].

ABSTRACT In this work, we provide a unified framework for full-duplex (FD) massive multiple-input multiple-output (MIMO) cellular networks with low-resolution analog-to-digital and digital-to-analog converters (ADCs and DACs). An objective of this work is to derive an accurate model to account for a wide variety of network irregularities and imperfections, including loopback self-interference (SI) that arises in full-duplex systems and quantization error from low-resolution data converters. Our contributions for forward and reverse links include (1) deriving signal-to-quantization-plus-interference-plus-noise ratio (SQINR) under pilot contamination, linear minimum mean square error (LMMSE) channel estimation and channel hardening; (2) deriving closed-form and approximate analytical expressions of spectral efficiency; (3) deriving asymptotic results and power scaling laws with respect to the number of quantization bits, base station antennas, and users, as well as base station and user equipment power budgets; and (4) analyzing outage probability and spectral efficiency vs. cell shape, shadowing, noise, cellular interference, pilot contamination, pilot overhead, and frequency reuse. Cell shapes include hexagonal, square, and Poisson Point Process (PPP) tessellations. In simulation, we quantify spectral and energy efficiency as well as the impact of SI power, inter-user interference, and cell shape on outage probability. We carry out the analysis for sub-7 GHz long term evolution (LTE) bands and then extend the framework to support millimeter wave (mmWave) bands.

INDEX TERMS Full-duplex, massive MIMO, low resolution ADC/DAC, cellular networks, interference, networks lattice/tessellation, LTE, mmWave.

I. INTRODUCTION

WITH increasing demand for higher data rate, lower latency, and higher reliability from a growing number of wireless users and services, radio frequency (RF) technologies seek to use the limited available spectrum more effectively. Beyond the connections from base stations to mobile and fixed wireless subscribers, cellular systems also provide backhaul from basestations to the Internet and other networks. Installing optical fiber or other cabling for backhaul can be prohibitively expensive and in some cases not allowed by law.

As far back as 2011, microwave and satellite RF bands had become commonly used to support backhaul [4]. Currently, millimeter wave (mmWave) technology, which refers to the spectrum in the 10-300 GHz range,[1] has emerged as a promising solution for providing large bandwidths. In particular, mmWave is an attractive band for integrated access and backhaul [5], [6], [7].

1. Although a rigorous definition of mmWave frequencies would place them between 30 and 300 GHz, industry has loosely defined them to include the spectrum from 10 to 300 GHz.

One proposed solution to address the scarcity of spectrum is to employ full-duplex (FD) transceivers [8]. FD systems have emerged as a viable solution to enable the efficient use of spectrum by allowing transmission and reception using the same resource blocks [9]. A direct consequence is the potential to reduce latency and overhead as well as double the spectral efficiency vs. half-duplex (HD) systems [10]. Moreover, FD transceivers are cost efficient since the transmit and receive arrays can be placed into a single dedicated array for shared transmission and reception [11], [12], [13]. These benefits call for the integration of FD into practical consideration, e.g., machine-to-machine communications as well as integrated access and backhaul which have been recently adopted in 3GPP Release 17 [14].

Due to the dramatic differences in received power from near and far transmitters, FD systems are constrained by loopback self-interference (SI) that leaks from the transmit array to the colocated receive array and that can be up to 100 dB stronger than the desired received signal [15], [16]. Without proper SI cancellation, the analog-to-digital converters (ADCs) can be swamped by SI, thereby resulting in very poor communication performance.

Recent publications have proposed robust beamforming design to suppress SI and enable FD operation [17], [18], [19]. Authors [20], [21], [22] have proposed beamforming techniques such as zero-forcing (ZF), minimum mean square error (MMSE), and null-space projection to suppress SI. In massive multiple-input multiple-output (MIMO) systems in particular, base stations (BSs) employ many more antennas than those available on user equipment (UE). Having a massive number of antennas enables not only enough spatial multiplexing gain but also sufficient degrees of freedom (DoF) to reduce SI and improve spectral efficiency significantly. In addition, authors in [23] investigated FD massive MIMO relaying with low resolution ADC in terms of spectral and energy efficiency. They derived the ZF as well as closed-form expressions for spectral efficiency and the tradeoff between energy and spectral efficiency for various system configurations. Moreover, work [24] proposed a beam-domain approach using hybrid time-switching and power splitting for FD massive MIMO systems to improve spectral efficiency. Furthermore, authors in [25] proposed an antenna selection scheme to cancel the loopback SI and used a genetic algorithm to solve the nonconvex optimization problem.

Several authors have harnessed the advantages of both FD and massive MIMO [26], [27], [28]. In fact, the authors in [26] and [27] investigated a multipair decode-and-forward relay employing FD massive MIMO and proved that as the number of antennas goes to infinity, SI is asymptotically suppressed. In [28], an SI-aware receive filter for the uplink (reverse link) and precoder for the downlink (forward link) are designed.

Although employing a massive number of antennas has many benefits, it comes with a tradeoff of hefty power consumption. In fact, having a large number of antennas leads to pronounced growth in the power consumption and hardware cost as each RF processing chain requires a pair of high-resolution ADCs (e.g., 10-12 bits each for commercial applications) [29], [30]. A b-bit ADC with a sampling frequency f_s requires $2^b \cdot f_s$ computations per second. Consequently, the power consumption grows exponentially with the resolution and linearly with the sampling frequency [31]. To circumvent this, low-resolution ADCs (1-3 bits) have been suggested for massive MIMO to reduce power consumption at the expense of spectral efficiency [32], [33], [34], [35], [36], [37].

Related works have proposed power-efficient system designs based on low-resolution ADCs and digital-to-analog converters (DACs). In [38], the authors investigated a FD massive MIMO amplify-and-forward relay with low-resolution ADCs while the authors in [39] studied a massive MIMO mixed-ADC system system, wherein a few of the high-resolution ADCs are allocated for channel estimation with 1-bit ADCs used for payload reception. In addition, the authors in [34] considered a mixed DAC/ADC multipair amplify-and-forward massive MIMO relay, analyzed sum spectral efficiency, and proposed a power allocation scheme with the aim of maximizing the sum spectral efficiency. An uplink spectral efficiency of a HD massive MIMO with low-resolution ADCs and a spectral/energy efficiency trade-off analysis in mixed ADC scenarios have been investigated over Rician channels in [29], [40], respectively.

In this paper, we propose a unified framework for analysis of FD massive MIMO cellular networks with low-resolution ADCs/DACs for different network topologies such as hexagonal lattice, square grid, and Poisson Point Process (PPP) tessellation. The BSs operate in FD mode under low-resolution ADCs/DACs and are each equipped with a massive number of antennas, while the UEs operate with a single antenna in HD mode under infinite ADC/DAC resolution. More importantly, we propose separate analysis frameworks for reverse and forward links under pilot contamination, and use matched filters in the receiver and for the precoder at the FD BSs. Since the BSs operate in FD, loopback SI is created at the BS transceiver wherein the precoded signal transmitted by the BS leaks to the BS combiner and consequently corrupts the uplink signals received from the users. In addition, downlink users are vulnerable to the inter-user interference (IUI) incurred by the uplink UEs since the BSs operate in FD mode.

To characterize the reverse and forward link performance measures, we evaluate the average signal-to-quantization-plus-interference-plus-noise ratio (SQINR)[2] among the users (either on the reverse or forward link). The channels are estimated in the reverse link phase wherein the UEs send the

2. The word "quantization" introduced in the term SQINR is derived from the application of low-resolution ADCs/DACs as the received signal becomes quantized rather than continuous in amplitude. Although the application of low-resolution ADCs/DACs reduces the power consumption, it incurs nonlinear distortion. One approach models the nonlinear distortion as additive noise. Other approach uses Bussgang Theory to linearize this distortion for the sake of simplicity and tractability and approximate the nonlinearity as a gain plus additive noise.

pilots to the BSs which estimate the channels and compute the precoders and combiners. We propose the forward link channel state information (CSI) acquisition based on the channel reciprocity property of time division duplex (TDD) systems. As long as the forward and reverse transmissions occur within the channel coherence time, the physical channel is reciprocal. This property is exploited for Massive MIMO [41] to avoid the large channel feedback to the BS in the reverse link phase. The only issue is that the receive and transmit RF chains in the transceivers (i.e., the hardware from the antenna to the ADC in the receive path and from the DAC to the antenna in the transmit path) are not reciprocal, thereby calibration is required to compensate hardware asymmetry. To facilitate the analysis, we assume TDD channel reciprocity with perfect calibration.

For channel modeling, we consider channel hardening; for channel estimation, we consider the linear minimum mean square error (LMMSE) approach. Capitalizing on both, we evaluate the cumulative distribution function (CDF), spectral efficiency, and energy efficiency vs. the average SQINR for reverse and forward links under several scenarios. To the best of our knowledge, this is the first work proposing a unified framework for FD massive MIMO in multiuser and multicell cases with low-resolution ADCs/DACs.

The main contributions of this work are summarized as follows:

- Derive expressions for the received signals as well as the relative SQINR for reverse and forward links under channel hardening, LMMSE channel estimation, low-resolution ADCs/DACs, and pilot contamination.
- Derive closed-form and approximate analytical expressions for spectral efficiency in the reverse and forward links. We adopt the additive quantization noise model (AQNM)[3] to model ADC and DAC quantization error. We show that the spectral efficiency is substantially affected by the use of low-resolution ADCs/DACs which cannot be compensated only by employing a massive number of BS antennas; each UE should adopt high resolution ADCs/DACs to ensure good performance. Since each UE only requires two ADCs for in-phase and quadrature (IQ) sampling in the reverse link and two DACs for IQ sampling in the forward link, using high-resolution data converters in the UEs is a viable solution.
- Analyze the effects of network imperfections and irregularities such as the cell shape, shadowing, noise and cellular interference on the reverse and forward links. Cellular interference includes pilot contamination as well as inter-cell and intra-cell interference. We further investigate the impact of pilot overhead, number of users per cell, and frequency reuse factor on both the CDF and spectral efficiency.
- Gauge the effects of full-duplexing such as SI channel power, SI signal power, and IUI on the reverse and forward link users, respectively.
- Derive asymptotic results as well as power scaling laws for reverse and forward links in order to unpack engineering insights into the proposed system model.
- Demonstrate the generality of the proposed work by showing the results match those in related work for several special cases. Although some of the special cases such as single-user, single-cell, and high-resolution cases, are less common, the analysis of these cases is useful for gaining insight.
- Assess the numerical results in terms of CDF, spectral and energy efficiency for hexagonal lattice, square grid and PPP tessellation.

The paper is organized as follows. The system model is introduced in Section II. The reverse and forward links analysis are presented in Sections III and IV, respectively. Derivation of asymptotic results as well as power scaling laws are reported in Section V. Section VI extends the modeling of the reverse and forward links from sub-7 GHz LTE bands to 5G LTE millimeter wave bands. Section VII defines performance measures of energy efficiency and outage probability. The numerical results and their discussion are presented in Section VIII while Section IX concludes the paper.

Notation: We use the following notation throughout this paper: bold lowercase $\mathbf{x}$ is used to denote column vectors, bold uppercase $\mathbf{X}$ is used to denote matrices, non-bold letters x, X are used to denote scalar values and calligraphic letters $\mathcal{X}$ to denote sets. Using this notation, $|x|$ is the absolute value of a scalar, $\|\mathbf{x}\|$ is the norm. $\mathbf{X}^*$ is the Hermitian or conjugate transpose, $\mathbf{X}^T$ is the matrix transpose, $\mathbf{X}^\dagger$ is the Moore-Penrose inverse, $\mathbf{X}^{-1}$ denotes the inverse of a square non-singular matrix, $[\mathbf{x}]_n$ is the n-th entry of $\mathbf{x}$, and $[\mathbf{X}]_{mn}$ is the element located in the m-th row and the n-th column in the matrix $\mathbf{X}$. We use $\mathcal{CN}(\mathbf{m}, \Sigma)$ to denote a complex circularly symmetric Gaussian random vector with mean $\mathbf{m}$ and covariance Σ. We use $\mathcal{U}[a, b]$ to denote the uniform distribution within the range $[a, b]$. We use $\mathbb{E}[\cdot]$ to denote the expectation and $\mathsf{var}[\cdot]$ to denote the variance. We denote subscripts u for uplink and d for downlink. Table 1 defines the mathematical symbols most commonly used in this paper.

II. NETWORK MODEL

We consider a macrocellular network where each BS operates in FD mode and is equipped with $N_\mathsf{a} \gg 1$ antennas. Each UE operates in half-duplex mode and has a single antenna.

A. NETWORK GEOMETRY

Recent research on modern cellular networks has proposed various approaches to address the modeling and performance analysis of reverse and forward links. The Wyner model [42] gained enormous attention for its simplicity as it considers inter-cell interference to be constant or a single random

3. To facilitate analytical performance of systems with low resolution ADCs/DACs, we adopt the common AQNM proposed in the literature.

TABLE 1. Definition of symbols commonly used in the paper in alphabetical order.

Variable	Symbol
Bandwidth	B
Number of ADC/DAC resolution bits	b
Fraction of pilot overhead	β
Set of cells reusing the same pilot dimensions	$\mathcal{C}$
Walden's figure of merit for ADCs and DACs	c
Shadowing (Variance)	$\chi(\sigma_{\mathsf{dB}})$
Copilot distance between the cell of interest and its first tier of copilot cells	D_{copilot}
Fractional frequency reuse factor	Δ
Pathloss exponent	η
Precoder applied from ℓ-th BS to k-th user in l-th cell	$\mathbf{f}_{\ell,(l,k)}$
Large scale fading between ℓ-th BS and the k-th user served by l-th BS	$G_{\ell,(k,l)}$
Small scale fading between the n-th user in ℓ-th cell and the k-th user in l-th cell	$\mathbf{g}_{(\ell,n),(l,k)}$
Self-interference channel	$\mathbf{H}_{\mathsf{SI}}$
Small scale fading between ℓ-th BS and the k-th user served by l-th BS	$\mathbf{h}_{\ell,(k,l)}$
LMMSE channel estimate	$\hat{\mathbf{h}}$
LMMSE channel estimation error	$\tilde{\mathbf{h}}$
Spectral efficiency of k-th user for matched filter	$\mathcal{I}_k^{\mathsf{MF}}$
Effective spectral efficiency	$\mathcal{I}^{\mathsf{eff}}$
Energy efficiency	$\mathcal{J}$
Number of users in ℓ-th cell	K_ℓ
BSs density	λ_{BS}
UEs density	λ_{UE}
Pathloss offset	L_{ref}
Self-interference channel power	μ_{SI}^2
Variance of LMMSE channel estimation error	MMSE
Number of antennas at BS	N_{a}
Number of coherence tiles	N_{c}
Number of pilots per cell	N_{p}
BSs location process	$\mathbf{\Phi}_{\mathsf{BS}}$
UEs location process	$\mathbf{\Phi}_{\mathsf{UE}}$
Power between ℓ-th BS and k-th user in l-th cell	$P_{\ell,(l,k)}$
Outage probability for a threshold ζ	$P_{\mathsf{out}}(\zeta)$
Self-interference power	P_{SI}
Maximum uplink (downlink) power	$P_u(P_d)$
Additive quantization noise	$\mathbf{q}$
Distance between ℓ-th BS and the k-th user served by l-th BS	$r_{\ell,(k,l)}$
Inverse of the signal-to-quantization-plus-noise ratio	ρ
Forward-to-reverse links SNR ratio	ϱ
Signal-to-interference-plus-noise ratio of k-th user	sinr_k
Signal-to-noise ratio from the cell of interest to k-th uplink (downlink) user	$\mathsf{SNR}_k^u(\mathsf{SNR}_k^d)$
Signal-to-noise ratio from ℓ-th BS to k-th user in l-th cell	$\mathsf{SNR}_{\ell,(l,k)}$
SNR between the k-th uplink user served by the BS of interest and the k-th downlink user served by the ℓ-th BS	$\mathsf{SNR}_{(\ell,\mathsf{k}),k}^{\mathsf{iui}}$
Signal-to-quantization-plus-interference-plus-noise ratio of k-th user	sqinr_k
SQINR of k-th user based on LMMSE channel estimation	$\mathbb{E}[\mathsf{sqinr}_k]$
SQINR of k-th user based on channel hardening	$\widetilde{\mathsf{sqinr}}_k$
Large scale fading between n-th user in ℓ-th BS and the k-th user in l-th BS	$T_{(\ell,n),(l,k)}$
Large scale fading between the ℓ-th BS and the k-th user in l-th BS	$G_{\ell,(l,k)}$
Shadowing between the ℓ-th BS and the k-th user in l-th BS	$\chi_{\ell,(l,k)}$
Noise (variance)	$\mathbf{v}(\sigma^2)$
Combiner at ℓ-th BS from the k-th user in l-th cell	$\mathbf{w}_{\ell,(l,k)}$
Precoded symbols vector transmitted by ℓ-th BS	$\mathbf{x}_\ell$
Power control (Reverse)/Power allocation (Forward)	ϑ

variable to account for fading. However, it has been shown in [43] that this model suffers from shortcomings in the cases where the inter-cell interference is spatially averaged, e.g., a code division multiple access (CDMA) network congested by a high load. In the same context, existing work suggests a network model consisting of regular and deterministic BS deployment, e.g., hexagonal or square grid-based model shown by Figs. 1 and 2(a). Although this network model is regular, closed-form expressions for the communication performance are not tractable and instead the derivation is based on approximations and Monte Carlo simulation. It has been shown that the grid-based model is an upper bound to the actual performance retrieved from real data, e.g., the signal-to-interference-plus-noise ratio (SINR) coverage based upon a square grid is an upper bound to network measurements [44], [45].

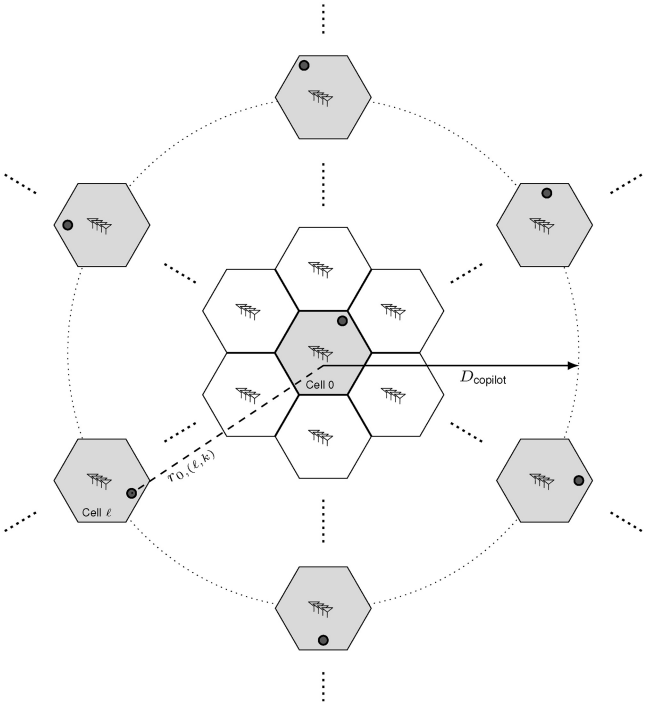

FIGURE 1. Hexagonal lattice network. The cell of interest and the cells belonging to subset $\mathcal{C}$, i.e., all the ones reusing the same pilot dimensions, are shaded and a copilot user equipment in each cell is indicated by a circle. Also indicated is the distance $r_{0,(\ell,k)}$ between the cell of interest cell 0 and the k-th user equipment served by the cell ℓ. In addition, indicated is the distance D_{copilot} between the cell of interest and its first tier of copilot cells.

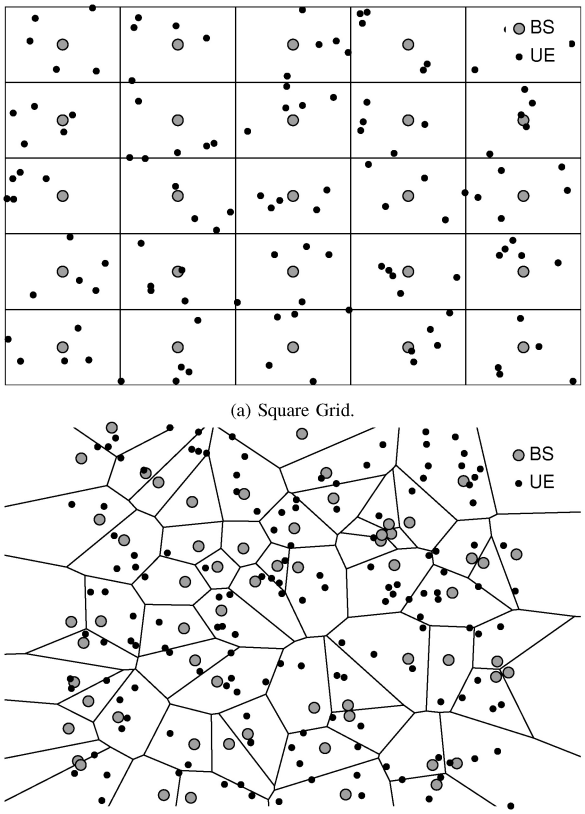

(a) Square Grid.

(b) PPP Voronoi Tessellation.

FIGURE 2. Realization of homogeneous cellular networks. (a) Square grid consists of regular deployment of BSs while the UEs are uniformly distributed in the cells. (b) PPP network model wherein the deployment of BSs and UEs are distributed according to a PPP.

Limitations of previous approaches led to the development of random spatial models for network modeling. This new perspective brought two important results. First, tractable derivations of communication performance such as rate and SINR expressions became possible. Second, random spatial models were at least as accurate as grid-based models and in many cases more accurate with respect to actual networks. For example, Fig. 2(b) is a PPP distribution of both BS deployment and UE locations, which provides accurate SINR statistics for real urban networks [46].

B. LARGE-SCALE FADING

The locations of BSs form a stationary and ergodic point process $\mathbf{\Phi}_{\text{BS}} \subset \mathbb{R}^2$ of density λ_{BS}, and the UE positions follow an independent point process $\mathbf{\Phi}_{\text{UE}} \subset \mathbb{R}^2$ of density λ_{UE}, which is also stationary and ergodic. Together, they model a realistic macrocellular network scenario.

Each UE is associated with the BS from which it has the strongest large-scale channel gain and we denote by K_ℓ^u and K_ℓ^d the number of uplink and downlink UEs served by the ℓ-th BS. The large-scale gain comprises pathloss with exponent $\eta > 2$ and shadowing that is independently and identically distributed (IID) across the paths. In particular, the large-scale gain between the ℓ-th BS and the k-th user connected to the l-th BS is

$$G_{\ell,(l,k)} = \frac{L_{\text{ref}}}{r_{\ell,(l,k)}^{\eta}} \chi_{\ell,(l,k)}, \tag{1}$$

with L_{ref} as the pathloss intercept at a unit distance, $r_{\ell,(l,k)}$ the link distance, and $\chi_{\ell,(l,k)}$ as the shadowing coefficient satisfying $\mathbb{E}[\chi^{2/\eta}] < \infty$. Further, we introduce large-scale fading between the UEs to model the IUI. We denote $T_{(\ell,n),(l,k)}$ as the large-scale channel gain between the n-th user and the k-th user associated with the ℓ-th and l-th BSs, respectively.

Without loss of generality, we denote the 0-th BS as the focus of interest and drop its subscript for notational compactness. For large-scale gains,

- $G_{0,(l,k)} = G_{(l,k)}$ relates the BS of interest with the k-th UE associated with the l-th BS.
- $G_{\ell,(0,k)} = G_{\ell,k}$ relates the ℓ-th BS with the k-th UE associated with the BS of interest.
- $G_{0,(0,k)} = G_k$ relates the BS of interest with its own k-th UE.
- $K_0 = K$ is the number of UEs served by the BS of interest.

The same scripting and compact notation are applied to other quantities.

C. SMALL-SCALE FADING

We denote $\mathbf{h}_{\ell,(l,k)} \sim \mathcal{N}_{\mathbb{C}}(\mathbf{0}, \mathbf{I})$ as the normalized reverse link $N_{\mathsf{a}} \times 1$ small-scale fading between the k-th user located in cell l and the BS in cell ℓ and $\mathbf{h}^*_{\ell,(l,k)}$ as the forward link

reciprocal, assuming TDD with perfect calibration [47]. In addition, we denote by $\mathbf{g}_{(\ell,n),(l,k)} \sim \mathcal{N}_{\mathbb{C}}(0, \sigma^2_{\text{iui}})$ the 1×1 small-scale fading between the n-th user in cell ℓ and the k-th user in cell l [32]. We further denote by $\mathbf{H}_{\mathsf{SI}} \sim \mathcal{N}_{\mathbb{C}}(\mathbf{0}, \mu^2_{\mathsf{SI}})$ the SI channel matrix ($N_{\mathsf{a}} \times N_{\mathsf{a}}$) [32].

Remark 1: In this work, we assume perfect knowledge of the SI channel. The estimation of the SI channel can be carried out with conventional methods such as Least Squares (LS) or MMSE estimators. If the channel matrix is sparse, then a compressive sensing method will be the best candidate, in particular, for a channel matrix of large dimension. In addition, we consider an estimate of the SI channel ($\hat{\mathbf{H}}_{\mathsf{SI}}$) while the estimation error can be accounted as additional source of SI. Note that tackling the SI channel estimation problem is out of the scope of this work.

D. NUMBER OF USERS PER CELL

Regardless of the regularity of the network lattice, disparities may come to play across the BSs due to shadowing and randomness of user locations.

Without shadowing, any user is associated with the tagged BS in its Voronoi cell, and the number of users, conditioned on the cell area, is a random variable with mean λ_{UE} multiplied by the cell area $\mathcal{A}$. If $\mathbf{\Phi}_{\mathsf{UE}}$ is a PPP, then the number of users follows a Poisson distribution. Depending on how the cell area is distributed, the distribution of the number of users per cell can be evaluated. For example, if $\mathbf{\Phi}_{\mathsf{UE}}$ is a PPP, such number in a lattice network is Poisson distributed with average $\lambda_{\mathsf{UE}}/\lambda_{\mathsf{BS}}$ while, for an irregular network with PPP distributed BSs, the corresponding distribution is approximated in [48].

In the presence of shadowing, a user is not necessarily associated with the nearest BS. Although the shadowing per link is strong and independent, the number of users per BS still follows a Poisson distribution with mean $\lambda_{\mathsf{UE}}/\lambda_{\mathsf{BS}}$ regardless of the BS locations. In fact, when shadowing increases significantly, it dominates the pathloss and each BS becomes equally likely to be the one serving a particular user. For instance, let's consider a region with a finite area $\mathcal{A}$ consisting of $\mathcal{A}\lambda_{\mathsf{BS}}$ BSs and $\mathcal{A}\lambda_{\mathsf{UE}}$ UEs, all located randomly. When the shadowing strengthens, the number of users served by each BS follows a Binomial distribution $\mathcal{B}(\mathcal{A}\lambda_{\mathsf{UE}}, \frac{1}{\mathcal{A}\lambda_{\mathsf{BS}}})$, since each UE has equal probability $\frac{1}{\mathcal{A}\lambda_{\mathsf{UE}}}$ of being associated with any of the $\mathcal{A}\lambda_{\mathsf{BS}}$ BSs. For a region with infinite area ($\mathcal{A} \longrightarrow \infty$) and with a constant mean $\lambda_{\mathsf{UE}}/\lambda_{\mathsf{BS}}$, the Binomial distribution converges to a Poisson distribution [49].

E. QUANTIZED SIGNAL MODEL

For signal amplitudes with infinite resolution, a typical received signal $\mathbf{y}$ is given by

$$\mathbf{y} = \mathbf{H}\mathbf{x} + \mathbf{n}, \tag{2}$$

where $\mathbf{H}$, $\mathbf{x}$, and $\mathbf{n}$ are the channel matrix, precoded symbols, and additive white Gaussian noise (AWGN), respectively.

TABLE 2. ρ for different values of b [54].

b	1	2	3	4	5
ρ	0.3634	0.1175	0.03454	0.009497	0.002499

For ADCs, many nonlinear quantization models have been proposed; however, the analysis of such models is complex for a higher number of bits of amplitude resolution. In quantized systems, a lower bound on the spectral efficiency has been derived by treating the quantization as additive Gaussian noise with variance inversely proportional to the resolution of the quantizer, i.e., 2^{-b} times the received input power where b is the number of ADC bits.

Recent work [10], [50], [51], [52] used an AQNM to model the nonlinear distortion as a gain plus additive noise for mmWave signals for an arbitrary number of ADC bits. In addition, authors in [53], [54], [55] derived Gaussian approximations using Bussgang Theory to linearize the nonlinear quantization distortion which is quite similar to the AQNM. The received signal (2) is processed by RF chains and then converted to the digital discrete-time domain by ADCs. The AQNM represents the quantized version of (2) given by

$$\mathbf{y}_q = \alpha\mathbf{y} + \mathbf{q}, \tag{3}$$

where $\mathbf{q}$ is the additive quantization noise, and $\alpha = 1 - \rho$ where ρ is the inverse of the signal-to-quantization-plus-noise ratio (SQNR), which is inversely proportional to the square of the resolution of an ADC, i.e., $\eta \propto 2^{-2b}$.

F. TIGHTNESS OF AQNM

We consider a uniform quantizer with step size Δ defined as $\Delta = \frac{b-a}{2^{\text{Bits}}-1}$ where a and b are the lower and upper bounds of the quantizer input. We denote by $\mathbf{y}_e$ as the output of the uniform quantizer and $\mathbf{y}_q$ as the quantized signal using the AQNM given by (3). In (3), $\mathbf{y}$ is the input of the quantizer, which is assumed to be uniformly distributed on $[a, b]$. Note that $\mathbf{q}$ is additive quantization noise which has a Gaussian distribution with zero mean and variance given by [56]

$$\sigma^2_q = \frac{\Delta^2}{12}, \tag{4}$$

The mean square error (MSE) is defined by

$$\text{MSE} = \sum_n \mathbb{E}\Big[|\mathbf{y}_e[n] - \mathbf{y}_q[n]|^2\Big]. \tag{5}$$

To show the tightness, let's consider an example of a quantizer with $a = -15V$ and $b = 15V$, $\mathbf{y} \sim \mathcal{U}[-15, 15]$. As shown by Fig. 3, as the number of quantization bits increases, the MSE decreases; i.e., the precision of the AQNM is accurate and the model gets closer to the output of the quantizer.

G. FULL-DUPLEX AND LOW RESOLUTION ADC/DAC

Fig. 4 illustrates a basic abstraction of a BS operating in FD mode. The uplink UEs send the data to the BS independently

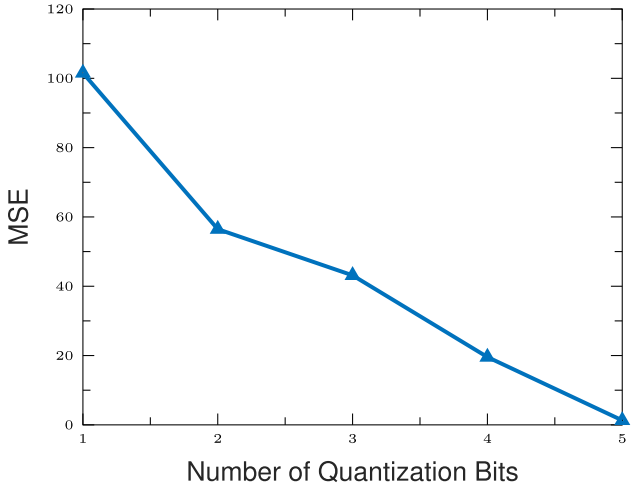

FIGURE 3. MSE between the output of the quantizer and quantized signal obtained using the AQNM.

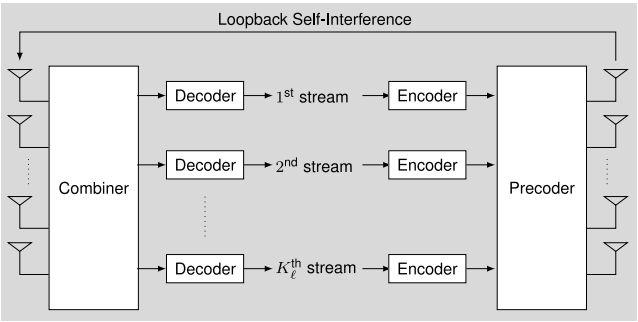

FIGURE 4. Basic abstraction of a full-duplex base station: The uplink user equipment (UE) sends the data to the base station (BS) independently from the data intended to the downlink UE sent from the BS. Since the BS transmits and receives simultaneously at the same resource blocks, SI leakage is created in the form of a loopback from TX to RX sides of the BS.

from the data intended for the downlink UE transmitted from the BS. Since the BS transmits and receives simultaneously using the same resource blocks, SI leakage is created as loopback from transmit (TX) to receive (RX) arrays of the BS.

Without loss of generality, we illustrate the analysis of a FD system with low resolution ADCs/DACs for a single-cell scenario. Then we generalize the analysis to a multi-cell network for reverse and forward links.

The received uplink signal $\mathbf{y}^u$ at the BS prior to quantization is given by

$$\mathbf{y}^u = \sqrt{P_u}\mathbf{H}_u\mathbf{x}_u + \sqrt{P_d}\mathbf{H}_{\mathsf{SI}}\mathbf{y}_q^d + \mathbf{n}_u, \tag{6}$$

where the downlink unquantized precoded signal $\mathbf{y}^d$ is given by

$$\mathbf{y}^d = \mathbf{F}\mathbf{x}_d. \tag{7}$$

Here, $\mathbf{F}$ is the precoder. By approximating the quantization effects using the AQNM, the received signal $\mathbf{y}^u$ and transmitted signal $\mathbf{y}^d$ after quantization at the BS can be modeled as

$$\mathbf{y}_q^u = \alpha_u\mathbf{y}^u + \mathbf{q}_u \tag{8}$$

$$\mathbf{y}_q^d = \alpha_d\mathbf{y}^d + \mathbf{q}_d. \tag{9}$$

We define the covariance matrices for the AQNM [32] as

$$\mathbf{R}_{\mathbf{q}_u} = \mathbb{E}\left[\mathbf{q}_u\mathbf{q}_u^*\right] = \alpha_u(1-\alpha_u)\,\mathrm{diag}\left(P_u\mathbf{H}_u\mathbf{H}_u^* + \mathbf{Q} + \sigma^2\mathbf{I}_{N_\mathsf{a}}\right) \tag{10}$$

$$\mathbf{R}_{\mathbf{q}_d} = \mathbb{E}\left[\mathbf{q}_d\mathbf{q}_d^*\right] = \alpha_d(1-\alpha_d)\,\mathrm{diag}\left(\mathbf{F}\mathbf{F}^*\right), \tag{11}$$

where $\mathbf{Q}$ is given by

$$\mathbf{Q} = P_u\mathbf{H}_{\mathsf{SI}}\left(\alpha_d^2\mathbf{F}\mathbf{F}^* + \mathbf{R}_{\mathbf{q}_d}\right)\mathbf{H}_{\mathsf{SI}}^*. \tag{12}$$

III. REVERSE LINK ANALYSIS

At the channel estimation stage, we assume the BS operates in HD mode with full-resolution ADCs and DACs [34]. In other words, in the absence of the SI and quantization error due to limited ADC/DAC resolution, the received signal (sent from the k-th uplink UE) at the BS of interest, assuming no pilot contamination and single-cell single-user case, is given by

$$\mathbf{y}_k^u = \sqrt{G_kP_k}\mathbf{h}_k + \mathbf{v}_k. \tag{13}$$

Upon data transmission from the users (in a multicell and multiuser scenario), the BS operates in full-duplex mode with low-resolution ADCs/DACs. Consequently, the BS of interest observes the following received signal vector

$$\mathbf{y}_q^u = \alpha_u\sum_{\ell}\sum_{k=0}^{K_\ell-1}\sqrt{G_{\ell,k}P_{\ell,k}}\mathbf{h}_{\ell,k}s_{\ell,k} + \alpha_u\sqrt{P_{\mathsf{SI}}}\mathbf{H}_{\mathsf{SI}}\mathbf{q}_d + \alpha_u\alpha_d\sqrt{P_{\mathsf{SI}}}\sum_{k=0}^{K-1}\mathbf{H}_{\mathsf{SI}}\mathbf{f}_ks_k^d + \mathbf{q}_u + \alpha_u\mathbf{v}. \tag{14}$$

Next, we will consider two channel estimation/acquisition approaches, LMMSE and channel hardening, wherein the pilot contamination will come to play.

Remark 2: As illustrated in Fig. 4, the BS consists of two antennas arrays dedicated for transmission and reception and hence the uplink and downlink channels estimation can be carried out separately.

A. LMMSE CHANNEL ESTIMATION

Decomposing the channel into an estimate and an error term entails a new formulation of the received signal vector

$$\mathbf{y}_q^u = \alpha_u\sum_{\ell}\sum_{k=0}^{K_\ell-1}\sqrt{G_{\ell,k}P_{\ell,k}}\left(\hat{\mathbf{h}}_{\ell,k} + \tilde{\mathbf{h}}_{\ell,k}\right)s_{\ell,k} + \alpha_u\mathbf{v} + \alpha_u\alpha_d\sqrt{P_{\mathsf{SI}}}\sum_{k=0}^{K-1}\mathbf{H}_{\mathsf{SI}}\mathbf{f}_ks_k^d + \alpha_u\sqrt{P_{\mathsf{SI}}}\mathbf{H}_{\mathsf{SI}}\mathbf{q}_d + \mathbf{q}_u. \tag{15}$$

Note that $\hat{\mathbf{h}}_{\ell,k}$ is the LMMSE channel estimate and $\tilde{\mathbf{h}}_{\ell,k}$ is the channel estimation error which is uncorrelated with the channel estimate and has variance given by

$$\mathsf{MMSE}_k = \frac{1}{1+\frac{P_k}{P_u}\mathsf{SNR}_k^u}, \tag{16}$$

where P_d is the total power transmitted from the BS at the cell of interest and P_k is the power transmitted from the k-th user to the BS of interest.

Since the number of coherence tiles N_{c} is finite,[4] the number of orthogonal pilot dimensions $N_{\mathsf{p}} < N_{\mathsf{c}}$ is also finite. While it is possible to assign orthogonal pilots to K active users in certain cells, it is impossible to preserve pilot orthogonality over the entire network especially when having many cells. When the system runs out of orthogonal pilots, pilots have to be reused across network cells. Eventually, this reuse incurs interference or *pilot contamination* during the estimation stage. For each user, the BS of interest would like to estimate the quantity

$$\sqrt{\frac{P_k}{P_u}}G_k\mathbf{h}_k,\ \ k=0,\ldots,K-1, \tag{17}$$

However, with pilot contamination, the BS ends up estimating

$$\sqrt{\frac{P_k}{P_u}}G_k\mathbf{h}_k+\sum_{\ell\in\mathcal{C}}\sqrt{\frac{P_{\ell,k}}{P_u}}G_{\ell,k}\mathbf{h}_{\ell,k},\ \ k=0,\ldots,K-1, \tag{18}$$

4. The number of coherence tiles per fading block or also termed as the number of single-carrier symbols per block denoted by $N_{\mathsf{c}}=BT_{\mathsf{c}}$, where B is the bandwidth and T_{c} is the channel coherence time. If the fading blocks are IID, then T_{c} coincides with the coherence time of a stationary fading process, which leads to $N_{\mathsf{c}}=\lceil\frac{B}{2\nu}\rceil$ with ν is the velocity. Note that the expressions of the number of coherence tiles hold if the bandwidth is not too large [57, Ch. 3].

Thereby, the LMMSE channel estimate is given

$$\hat{\mathbf{h}}_k=\frac{\frac{P_k}{P_u}\mathsf{SNR}_k^u}{1+\frac{P_k}{P_u}\mathsf{SNR}_k^u+\sum_{\ell\in\mathcal{C}}\frac{P_{\ell,k}}{P_u}\mathsf{SNR}_{\ell,k}^u}\times\left(\mathbf{h}_k+\sum_{\ell\in\mathcal{C}}\sqrt{\frac{\frac{P_{\ell,k}}{P_u}\mathsf{SNR}_{\ell,k}^u}{\frac{P_k}{P_u}\mathsf{SNR}_k^u}}\mathbf{h}_{\ell,k}+\mathbf{v}_k'\right), \tag{19}$$

and the variance of the LMMSE channel estimation error $\tilde{\mathbf{h}}_k$ becomes

$$\mathsf{MMSE}_k=\frac{1+\sum_{\ell\in\mathcal{C}}\frac{P_{\ell,k}}{P_u}\mathsf{SNR}_{\ell,k}^u}{1+\frac{P_k}{P_u}\mathsf{SNR}_k^u+\sum_{\ell\in\mathcal{C}}\frac{P_{\ell,k}}{P_u}\mathsf{SNR}_{\ell,k}^u}. \tag{20}$$

Proof: The proof is given in Appendix A. ■

B. DATA TRANSMISSION

By decomposing the interference into inter-cell and intra-cell components and applying the linear receive filter $\mathbf{w}_k^*$ at the k-th user ($y_{q,k}^u=\mathbf{w}_k^*\mathbf{y}_q^u$), the received signal at the BS of interest of the k-th user is given by (21), shown at the bottom of the page. To distinguish pilot contamination from other sources of interference, we decompose the sources of inter-cell interference which results in the expression of the received signal (22), shown at the bottom of the page.

Theorem 1: For LMMSE channel estimation, the output SQINR of the k-th uplink user is given by (23).

$$\mathsf{sqinr}_k=\frac{\alpha_u^2\frac{P_k}{P_u}\mathsf{SNR}_k^u|\mathbf{w}_k^*\hat{\mathbf{h}}_k|^2}{\mathsf{den}_u}, \tag{23}$$

where den_u is given by (24), shown at the bottom of the next page.

$$y_{q,k}^u=\underbrace{\alpha_u\sqrt{G_kP_k}\mathbf{w}_k^*\hat{\mathbf{h}}_ks_k}_{\text{Desired Signal}}+\underbrace{\alpha_u\sqrt{G_kP_k}\mathbf{w}_k^*\tilde{\mathbf{h}}_ks_k}_{\text{Channel Estimation Error}}+\underbrace{\alpha_u\sum_{\mathrm{k}=0}^{K-1}\sqrt{G_kP_{\mathrm{k}}}\mathbf{w}_k^*\left(\hat{\mathbf{h}}_k+\tilde{\mathbf{h}}_k\right)s_{\mathrm{k}}}_{\text{Intra-Cell Interference}}+\underbrace{\alpha_u\sum_{\ell\neq0}\sum_{\mathrm{k}=0}^{K_\ell-1}\sqrt{G_{\ell,k}P_{\ell,\mathrm{k}}}\mathbf{w}_k^*\mathbf{h}_{\ell,k}s_{\ell,\mathrm{k}}}_{\text{Inter-Cell Interference}}$$
$$+\underbrace{\alpha_u\alpha_d\sqrt{P_{\mathsf{SI}}}\sum_{\mathrm{k}=0}^{K-1}\mathbf{w}_k^*\mathbf{H}_{\mathsf{SI}}\mathbf{f}_{\mathrm{k}}s_{\mathrm{k}}^d}_{\text{Self-Interference due to Full-Duplexing}}+\underbrace{\alpha_u\sqrt{P_{\mathsf{SI}}}\mathbf{w}_k^*\mathbf{H}_{\mathsf{SI}}\mathbf{q}_d+\mathbf{w}_k^*\mathbf{q}_u}_{\text{Aggregate AQNM}}+\underbrace{\alpha_u\mathbf{w}_k^*\mathbf{v}}_{\text{Filtered Noise}} \tag{21}$$

$$y_{q,k}^u=\underbrace{\alpha_u\sqrt{G_kP_k}\mathbf{w}_k^*\hat{\mathbf{h}}_ks_k}_{\text{Desired Signal}}+\underbrace{\alpha_u\sqrt{G_kP_k}\mathbf{w}_k^*\tilde{\mathbf{h}}_ks_k}_{\text{Channel Estimation Error}}+\underbrace{\alpha_u\sum_{\mathrm{k}\neq k}\sqrt{G_kP_{\mathrm{k}}}\mathbf{w}_k^*\left(\hat{\mathbf{h}}_k+\tilde{\mathbf{h}}_k\right)s_{\mathrm{k}}}_{\text{Intra-Cell Interference}}+\underbrace{\alpha_u\sum_{\ell\in\mathcal{C}}\sqrt{G_{\ell,k}P_{\ell,k}}\mathbf{w}_{\ell,k}^*\mathbf{h}_{\ell,k}s_{\ell,k}}_{\text{Pilot Contamination}}$$
$$+\underbrace{\alpha_u\sum_{\substack{\ell\neq0\\\ell\notin\mathcal{C}}}\sum_{\mathrm{k}=0}^{K_\ell-1}\sqrt{G_{\ell,k}P_{\ell,\mathrm{k}}}\mathbf{w}_{\ell,\mathrm{k}}^*\mathbf{h}_{\ell,k}s_{\ell,\mathrm{k}}+\alpha_u\sum_{\ell\in\mathcal{C}}\sum_{\substack{\mathrm{k}=0\\\mathrm{k}\neq k}}^{K_\ell-1}\sqrt{G_{\ell,k}P_{\ell,\mathrm{k}}}\mathbf{w}_{\ell,\mathrm{k}}^*\mathbf{h}_{\ell,k}s_{\ell,\mathrm{k}}}_{\text{Inter-Cell Interference}}+\underbrace{\alpha_u\alpha_d\sqrt{P_{\mathsf{SI}}}\sum_{\mathrm{k}=0}^{K-1}\mathbf{w}_k^*\mathbf{H}_{\mathsf{SI}}\mathbf{f}_{\mathrm{k}}s_{\mathrm{k}}^d}_{\text{Self-Interference due to Full-Duplexing}}$$
$$+\underbrace{\alpha_u\sqrt{P_{\mathsf{SI}}}\mathbf{w}_k^*\mathbf{H}_{\mathsf{SI}}\mathbf{q}_d+\mathbf{w}_k^*\mathbf{q}_u}_{\text{Aggregate AQNM}}+\underbrace{\alpha_u\mathbf{w}_k^*\mathbf{v}}_{\text{Filtered Noise}} \tag{22}$$

Proof: The proof is given in Appendix B. ■

If the channel estimation is perfect, the pilot contamination is negligible and inter-cell interference is subsumed within the noise.

Proposition 1: With perfect CSI, without full-duplexing ($\mathbf{H}_{\mathsf{SI}} = \mathbf{0}$) and without pilot contamination, we retrieve the same SQINR expression for reverse link derived by [58].

Averaging over the channel realization $\hat{\mathbf{h}}_k$ and hence $\mathbf{w}_k$, the reverse link user spectral efficiency is provided by

$$\frac{\mathcal{I}_k}{B} = \mathbb{E}\big[\log\big(1+\mathsf{sqinr}_k\big)\big],\ k=0,\ldots,K-1, \tag{25}$$

If we introduce the pilot overhead, we would need to aggregate the reverse and forward spectral efficiencies or, in its place, a partition of the overhead between the reverse and forward links. Thereby, the effective reverse link spectral efficiency becomes

$$\frac{\mathcal{I}_k^{\mathsf{eff}}}{B} = \left(1-\beta\frac{N_{\mathsf{p}}}{N_{\mathsf{c}}}\right)\mathbb{E}\big[\log\big(1+\mathsf{sqinr}_k\big)\big],\ k=0,\ldots,K-1. \tag{26}$$

where $\beta \in [0,1]$ is the fraction of the pilot overhead ascribed to the reverse link.

C. CHANNEL HARDENING

One of the benefits of having massive number of antennas is the hardening of the filtered signals. Suppose that, rather than $\mathbf{w}_k^*\hat{\mathbf{h}}_k$ (where $\hat{\mathbf{h}}$ is the estimate of $\mathbf{h}$), the decoder regards $\mathbb{E}[\mathbf{w}_k^*\mathbf{h}_k]$ as the filtered channel. The receiver can compute this value from the channel statistics while the fluctuation of the filtered signal around the mean can be treated as SI. Thereby, (22) becomes (27) shown at the bottom of the page. When considering pilot contamination, the received signal of the k-th user can be reformulated as (28) shown at the bottom of the page.

Theorem 2: For channel hardening, the output SQINR of the k-th uplink user is given by

$$\overline{\mathsf{sqinr}}_k = \frac{\alpha_u^2\frac{P_k}{P_u}\mathsf{SNR}_k^u\big|\mathbb{E}\big[\mathbf{w}_k^*\mathbf{h}_k\big]\big|^2}{\overline{\mathsf{den}}_u}, \tag{29}$$

$$\mathsf{den}_u = \alpha_u^2\left(1+\sum_{\mathrm{k}\neq k}\frac{P_{\mathrm{k}}}{P_u}\mathsf{SNR}_{\mathrm{k}}^u\mathsf{MMSE}_{\mathrm{k}}+\sum_{\substack{\ell\neq 0\\ \ell\notin\mathcal{C}}}\frac{P_{\ell,\mathrm{k}}}{P_u}\mathsf{SNR}_{\ell,\mathrm{k}}^u+\sum_{\ell\in\mathcal{C}}\sum_{\substack{\mathrm{k}=0\\ \mathrm{k}\neq k}}^{K_\ell-1}\frac{P_{\ell,\mathrm{k}}}{P_u}\mathsf{SNR}_{\ell,\mathrm{k}}^u\right)\|\mathbf{w}_k\|^2+\alpha_u^2\sum_{\mathrm{k}\neq k}\frac{P_{\mathrm{k}}}{P_u}\mathsf{SNR}_k^u\left|\mathbf{w}_k^*\hat{\mathbf{h}}_{\mathrm{k}}\right|^2$$
$$+\alpha_u^2\sum_{\ell\in\mathcal{C}}\frac{P_{\ell,k}}{P_u}\mathsf{SNR}_{\ell,k}^u\mathbf{w}_k^*\mathbb{E}\big[\mathbf{h}_{\ell,k}\mathbf{h}_{\ell,k}^*|\mathbf{w}_k\big]\mathbf{w}_k+\frac{\alpha_u^2\alpha_d^2}{\sigma^2}P_{\mathsf{SI}}\sum_{\mathrm{k}=0}^{K-1}\left|\mathbf{w}_k^*\mathbf{H}_{\mathsf{SI}}\mathbf{f}_{\mathrm{k}}\right|^2+\frac{\alpha_u^2}{\sigma^2}P_{\mathsf{SI}}\left|\mathbf{w}_k^*\mathbf{H}_{\mathsf{SI}}\mathbf{q}_d\right|^2+\frac{1}{\sigma^2}\left|\mathbf{w}_k^*\mathbf{q}_u\right|^2 \tag{24}$$

$$y_{q,k}^u = \underbrace{\alpha_u\sqrt{G_kP_k}\mathbb{E}\big[\mathbf{w}_k^*\mathbf{h}_k\big]s_k}_{\text{Desired Signal}}+\underbrace{\alpha_u\sum_{\mathrm{k}\neq k}\sqrt{G_kP_{\mathrm{k}}}\mathbf{w}_k^*\mathbf{h}_ks_{\mathrm{k}}}_{\text{Intra-Cell Interference}}+\underbrace{\alpha_u\sum_{\ell\neq 0}\sum_{\mathrm{k}=0}^{K_\ell-1}\sqrt{G_{\ell,k}P_{\ell,\mathrm{k}}}\mathbf{w}_k^*\mathbf{h}_{\ell,k}s_{\ell,\mathrm{k}}}_{\text{Inter-Cell Interference}}+\underbrace{\alpha_u\sqrt{P_{\mathsf{SI}}}\mathbf{w}_k^*\mathbf{H}_{\mathsf{SI}}\mathbf{q}_d+\mathbf{w}_k^*\mathbf{q}_u}_{\text{Aggregate AQNM}}$$
$$\overbrace{+\underbrace{\alpha_u\sqrt{G_kP_k}\big(\mathbf{w}_k^*\mathbf{h}_k-\mathbb{E}\big[\mathbf{w}_k^*\mathbf{h}_k\big]\big)s_k}_{\text{Channel Estimation Error}}+\underbrace{\alpha_u\alpha_d\sqrt{P_{\mathsf{SI}}}\sum_{\mathrm{k}=0}^{K-1}\mathbf{w}_k^*\mathbf{H}_{\mathsf{SI}}\mathbf{f}_{\mathrm{k}}s_{\mathrm{k}}^d}_{\text{Self-Interference due to Full-Duplexing}}+\underbrace{\alpha_u\mathbf{w}_k^*\mathbf{v}}_{\text{Filtered Noise}}}^{\text{Aggregate Self-Interference}} \tag{27}$$

$$y_{q,k}^u = \underbrace{\alpha_u\sqrt{G_kP_k}\mathbb{E}\big[\mathbf{w}_k^*\mathbf{h}_k\big]s_k}_{\text{Desired Signal}}+\underbrace{\alpha_u\sqrt{G_kP_k}\big(\mathbf{w}_k^*\mathbf{h}_k-\mathbb{E}\big[\mathbf{w}_k^*\mathbf{h}_k\big]\big)s_k}_{\text{Channel Estimation Error}}+\underbrace{\alpha_u\sum_{\mathrm{k}\neq k}\sqrt{G_kP_{\mathrm{k}}}\mathbf{w}_k^*\mathbf{h}_ks_{\mathrm{k}}}_{\text{Intra-Cell Interference}}+\underbrace{\alpha_u\sum_{\ell\in\mathcal{C}}\sqrt{G_{\ell,k}P_{\ell,k}}\mathbf{w}_k^*\mathbf{h}_{\ell,k}s_{\ell,k}}_{\text{Pilot Contamination}}$$
$$\underbrace{+\alpha_u\sum_{\substack{\ell\neq 0\\ \ell\notin\mathcal{C}}}\sum_{\mathrm{k}=0}^{K_\ell-1}\sqrt{G_{\ell,k}P_{\ell,\mathrm{k}}}\mathbf{w}_k^*\mathbf{h}_{\ell,k}s_{\ell,\mathrm{k}}+\alpha_u\sum_{\ell\in\mathcal{C}}\sum_{\substack{\mathrm{k}=0\\ \mathrm{k}\neq k}}^{K_\ell-1}\sqrt{G_{\ell,k}P_{\ell,k}}\mathbf{w}_k^*\mathbf{h}_{\ell,k}s_{\ell,\mathrm{k}}+}_{\text{Inter-Cell Interference}}\underbrace{\alpha_u\alpha_d\sqrt{P_{\mathsf{SI}}}\sum_{\mathrm{k}=0}^{K-1}\mathbf{w}_k^*\mathbf{H}_{\mathsf{SI}}\mathbf{f}_{\mathrm{k}}s_{\mathrm{k}}^d}_{\text{Self-Interference due to Full-Duplexing}}$$
$$+\underbrace{\alpha_u\sqrt{P_{\mathsf{SI}}}\mathbf{w}_k^*\mathbf{H}_{\mathsf{SI}}\mathbf{q}_d+\mathbf{w}_k^*\mathbf{q}_u}_{\text{Aggregate AQNM}}+\underbrace{\alpha_u\mathbf{w}_k^*\mathbf{v}}_{\text{Filtered Noise}} \tag{28}$$

where $\overline{\mathsf{den}}_u$ is given by (30), shown at the bottom of the page. With $\overline{\mathsf{sqinr}}_k$, $k = 0, \ldots K-1$ being locally stable, the evaluation of the gross spectral efficiencies do not require averaging over the fading realizations, but rather it is directly computed by

$$\frac{\bar{\mathcal{I}}_k}{B} = \log\left(1 + \overline{\mathsf{sqinr}}_k\right), \quad k = 0, \ldots, K-1. \tag{31}$$

D. MATCHED FILTER RECEIVER

A matched filter for user k satisfies $\mathbf{w}_k^{\mathsf{MF}} \propto \hat{\mathbf{h}}_k$. This entails the following expression as [57, eq. (10.48)]

$$\mathbf{w}_k^{\mathsf{MF}} = \sqrt{\frac{\frac{P_k}{P_u}\mathsf{SNR}_k^u}{1 + \frac{P_k}{P_u}\mathsf{SNR}_k^u + \sum_{\ell\in\mathcal{C}}\frac{P_{\ell,k}}{P_u}\mathsf{SNR}_{\ell,k}^u}} \times \left(\mathbf{h}_k + \sum_{\ell\in\mathcal{C}}\sqrt{\frac{\frac{P_{\ell,k}}{P_u}\mathsf{SNR}_{\ell,k}^u}{\frac{P_k}{P_u}\mathsf{SNR}_k^u}}\mathbf{h}_{\ell,k} + \mathbf{v}_k'\right). \tag{32}$$

In above equation, the scaling is important to operate the decoder, but immaterial otherwise because it equally affects the received signal as well as the noise and interference. The scaling satisfies $\mathbb{E}[\|\mathbf{w}_k^{\mathsf{MF}}\|^2] = N_{\mathsf{a}}$ and the entries of $\mathbf{v}_k'$ have power of $1/(\frac{P_k}{P_u}\mathsf{SNR}_k^u)$ as discussed in [57, Sec. 10.3.2]. The pilots are assumed to be regular and aligned at every cell.

Corollary 1: If $\mathbf{x}$ and $\mathbf{y}$ are jointly Gaussian, i.e.,

$$\begin{bmatrix}\mathbf{y}\\ \mathbf{x}\end{bmatrix} \sim \mathcal{N}_{\mathbb{C}}\left(\begin{bmatrix}\mu_{\mathbf{y}}\\ \mu_{\mathbf{x}}\end{bmatrix}, \begin{bmatrix}\mathbf{R}_{\mathbf{y}} & \mathbf{R}_{\mathbf{yx}}\\ \mathbf{R}_{\mathbf{xy}} & \mathbf{R}_{\mathbf{x}}\end{bmatrix}\right) \tag{33}$$

The random variable $\mathbf{y}|\mathbf{x} = \mathsf{x}$ is complex Gaussian with mean

$$\mu = \mathbf{R}_{\mathbf{yx}}\mathbf{R}_{\mathbf{x}}^{-1}\mathsf{x} \tag{34}$$

and covariance

$$\mathbf{R} = \mathbf{R}_{\mathbf{y}} - \mathbf{R}_{\mathbf{yx}}\mathbf{R}_{\mathbf{x}}^{-1}\mathbf{R}_{\mathbf{xy}}. \tag{35}$$

We will use Corollary 1 later to prove the results of Theorem 3.

1) LMMSE CHANNEL ESTIMATION

In this subsubsection, we will derive the output SQINR of the k-th uplink user under LMMSE channel estimation and with a matched filter receiver.

Theorem 3: For LMMSE channel estimation and with a matched filter receiver, the output SQINR of the k-th uplink user is given by (36).

$$\mathsf{sqinr}_k^{\mathsf{MF}} = \frac{\alpha_u^2\frac{P_k}{P_u}\mathsf{SNR}_k^u|\mathbf{w}_k^{\mathsf{MF}*}\hat{\mathbf{h}}_k|^2}{\mathsf{den}_u^{\mathsf{MF}}} \tag{36}$$

where $\mathsf{den}_u^{\mathsf{MF}}$ is given by (37), shown at the bottom of the page.

Proof: The proof of Theorem 3 is given by Appendix C. ■

Proposition 2: With LMMSE channel estimation, without full-duplexing, with full-resolution ($\alpha_u = \alpha_d = 1$) and with a matched filter receiver, we exactly retrieve the same output SINR of the k-th uplink user given by [57, eq. (10.50)].

2) CHANNEL HARDENING

We adopt the matched filter receiver to design the combiner $\mathbf{w}_k$, $k = 0, \ldots, K^u - 1$.

Corollary 2: The matched filter receiver $\mathbf{w}_k^{\mathsf{MF}}$ (transmitter $\mathbf{f}_k^{\mathsf{MF}}$) has the following properties [32], [47]

1) $\mathbb{E}[\|\mathbf{w}_k^{\mathsf{MF}}\|^2] = \mathbb{E}[\|\mathbf{f}_k^{\mathsf{MF}}\|^2] = N_{\mathsf{a}}$.
2) $\mathbb{E}[\|\mathbf{w}_k^{\mathsf{MF}}\|^4] = \mathbb{E}[\|\mathbf{f}_k^{\mathsf{MF}}\|^4] = N_{\mathsf{a}}^2 + N_{\mathsf{a}}$.
3) $\mathbb{E}[|\mathbf{w}_k^{\mathsf{MF}*}\mathbf{h}_{\mathrm{k}}|^2] = \mathbb{E}[|\mathbf{h}_{\mathrm{k}}^*\mathbf{f}_k^{\mathsf{MF}}|^2] = N_{\mathsf{a}}$.

$$\begin{aligned}\overline{\mathsf{den}}_u = {}& \alpha_u^2\frac{P_k}{P_u}\mathsf{SNR}_k^u\mathsf{var}\left[\mathbf{w}_k^*\mathbf{h}_k\right] + \alpha_u^2\sum_{\mathrm{k}\neq k}\frac{P_{\mathrm{k}}}{P_u}\mathsf{SNR}_{\mathrm{k}}^u\mathbb{E}\left[\left|\mathbf{w}_k^*\mathbf{h}_{\mathrm{k}}\right|^2\right] + \alpha_u^2\sum_{\ell\in\mathcal{C}}\frac{P_{\ell,k}}{P_u}\mathsf{SNR}_{\ell,k}^u\mathbb{E}\left[\left|\mathbf{w}_k^*\mathbf{h}_{\ell,\mathrm{k}}\right|^2\right]\\ &+ \alpha_u^2\left(1 + \sum_{\substack{\ell\neq 0\\ \ell\notin\mathcal{C}}}\sum_{\mathrm{k}=0}^{K_\ell-1}\frac{P_{\ell,\mathrm{k}}}{P_u}\mathsf{SNR}_{\ell,k}^u + \sum_{\ell\in\mathcal{C}}\sum_{\substack{\mathrm{k}=0\\ \mathrm{k}\neq k}}^{K_\ell-1}\frac{P_{\ell,\mathrm{k}}}{P_u}\mathsf{SNR}_{\ell,\mathrm{k}}^u\right)\mathbb{E}\left[\|\mathbf{w}_k\|^2\right] + \frac{\alpha_u^2}{\sigma^2}P_{\mathsf{SI}}\mathbb{E}\left[|\mathbf{w}_k^*\mathbf{H}_{\mathsf{SI}}\mathbf{q}_d|^2\right]\\ &+ \frac{\alpha_d^2\alpha_u^2}{\sigma^2}P_{\mathsf{SI}}\sum_{\mathrm{k}=0}^{K-1}\mathbb{E}\left[\left|\mathbf{w}_k^*\mathbf{H}_{\mathsf{SI}}\mathbf{f}_{\mathrm{k}}\right|^2\right] + \frac{\alpha_u^2}{\sigma^2}\mathbb{E}\left[|\mathbf{w}_k^*\mathbf{q}_u|^2\right]\end{aligned} \tag{30}$$

$$\begin{aligned}\mathsf{den}_u^{\mathsf{MF}} = {}& \alpha_u^2\sum_{\mathrm{k}\neq k}\frac{P_{\mathrm{k}}}{P_u}\mathsf{SNR}_{\mathrm{k}}^u|\mathbf{w}_k^{\mathsf{MF}*}\hat{\mathbf{h}}_{\mathrm{k}}|^2 + \alpha_u^2\left(1 + \sum_{\mathrm{k}=0}^{K-1}\frac{P_{\mathrm{k}}}{P_u}\mathsf{SNR}_{\mathrm{k}}^u\mathsf{MMSE}_{\mathrm{k}} + \sum_{\ell\neq 0}\sum_{\mathrm{k}=0}^{K-1}\frac{P_{\ell,\mathrm{k}}}{P_u}\mathsf{SNR}_{\ell,\mathrm{k}}^u\right)\left\|\mathbf{w}_k^{\mathsf{MF}}\right\|^2\\ &+ \alpha_u^2\frac{\sum_{\ell\in\mathcal{C}}\left(\frac{P_{\ell,k}}{P_u}\mathsf{SNR}_{\ell,k}\right)^2}{1 + \frac{P_k}{P_u}\mathsf{SNR}_k^u + \sum_{\ell\in\mathcal{C}}\frac{P_{\ell,k}}{P_u}\mathsf{SNR}_{\ell,k}^u}\left(\left\|\mathbf{w}_k^{\mathsf{MF}}\right\|^4 - \left\|\mathbf{w}_k^{\mathsf{MF}}\right\|^2\right) + \frac{\alpha_u^2\alpha_d^2}{\sigma^2}P_{\mathsf{SI}}\sum_{\mathrm{k}=0}^{K-1}\left|\mathbf{w}_k^{\mathsf{MF}*}\mathbf{H}_{\mathsf{SI}}\mathbf{f}_{\mathrm{k}}\right|^2\\ &+ \frac{\alpha_u^2}{\sigma^2}P_{\mathsf{SI}}\left|\mathbf{w}_k^{\mathsf{MF}*}\mathbf{H}_{\mathsf{SI}}\mathbf{q}_d\right|^2 + \frac{1}{\sigma^2}\left|\mathbf{w}_k^{\mathsf{MF}*}\mathbf{q}_u\right|^2\end{aligned} \tag{37}$$

Theorem 4: For channel hardening and a matched filter receiver, the output SQINR of the k-th uplink user is given by (38).

$$\overline{\mathsf{sqinr}}_k^{\mathsf{MF}} = \frac{\alpha_u^2 \left(\frac{P_k}{P_u}\mathsf{SNR}_k^u\right)^2 N_{\mathsf{a}}^2}{\left(1+\frac{P_k}{P_u}\mathsf{SNR}_k^u + \sum_{\ell\in\mathcal{C}}\frac{P_{\ell,k}}{P_u}\mathsf{SNR}_{\ell,k}^u\right)\overline{\mathsf{den}}_u^{\mathsf{MF}}} \tag{38}$$

where $\overline{\mathsf{den}}_u^{\mathsf{MF}}$ is given by (39), as shown at the bottom of the page. Here, $\mathsf{INR} = P_{\mathsf{SI}}\mu_{\mathsf{SI}}^2/\sigma^2$.

Proof: The proof of Theorem 4 is provided in Appendix D ∎

Corollary 3: To further characterize the spectral efficiency, we derive a new bound using the following formula [59, eq. (35)]. Assuming statistical independence between x and y, we have

$$\mathbb{E}\left[\log\left(1+\frac{x}{y}\right)\right] \cong \log\left(1+\frac{\mathbb{E}[x]}{\mathbb{E}[y]}\right). \tag{40}$$

Lemma 1: Assuming perfect CSI, and applying Corollary 3, the output SQINR of the k-th uplink user (38) becomes

$$\overline{\mathsf{sqinr}}_k^{\mathsf{MF}} = \frac{\left(\frac{P_k}{P_u}\mathsf{SNR}_k^u\right)^2 (N_{\mathsf{a}}^2 + N_{\mathsf{a}})}{\left(1+\frac{P_k}{P_u}\mathsf{SNR}_k^u + \sum_{\ell\in\mathcal{C}}\frac{P_{\ell,k}}{P_u}\mathsf{SNR}_{\ell,k}^u\right)\overline{\mathsf{den}}_u^{\mathsf{MF}}}. \tag{41}$$

In the proof of Theorem 4 in Appendix D, the terms in (96), shown at the bottom of p. 25 related to the channel estimation error and pilot contamination vanish because the CSI is perfect.

Proposition 3: Considering a single-cell multiuser system (without any inter-cell interference) with perfect CSI, Corollary 3 entails the results for the reverse link in [32].

Proposition 4: With channel hardening, without full-duplexing, with full-resolution and with a matched filter receiver, the output SINR of the k-th uplink user is given by (42), shown at the bottom of the page.

Remark 3: Note that Proposition 4 entails the same result for reverse link derived in [57, eq. (10.63)].

Lemma 2: When the power (SNR_k^u) of the k-th uplink user goes to infinity, the output SINR (42) converges to N_{a}.

This SINR limit, caused by the channel estimation error, is incurred by the users with favorable conditions, i.e., having small shadowing and short distances from the associated BS. However, this limit is irreducible and cannot be overtaken by a matched filter receiver reliant on channel hardening.

Neglecting pilot contamination, the output SINR expression (42) can be reduced to

$$\overline{\mathsf{sinr}}_k^{\mathsf{MF}} \approx \frac{N_{\mathsf{a}}\left(\frac{P_k}{P_u}\mathsf{SNR}_k^u\right)^2}{\left(1+\frac{P_k}{P_u}\mathsf{SNR}_k^u\right)\left(1+\sum_\ell\sum_{\mathrm{k}=0}^{K_\ell^u-1}\frac{P_{\ell,k}}{P_u}\mathsf{SNR}_{\ell,\mathrm{k}}^u\right)}. \tag{43}$$

E. FRACTIONAL POWER CONTROL

In an outdoor environment, the received power is highly degraded by pathloss and shadowing; hence, we adopt a slow power control regime such as fractional power control to compensate pathloss. Such a power adaptation technique is characterized by a parameter $\vartheta \in [0,1]$ to control the received power of the UEs. Formally, $\frac{P_{\ell,0}}{P_u},\ldots,\frac{P_{\ell,K_\ell^u-1}}{P_u}$ must be optimized at each cell ℓ on the basis of that cell's weighted sum spectral efficiency. Consequently, the power control factor is

$$\frac{P_{\ell,k}}{P_u} \propto \frac{1}{G_{\ell,(\ell,k)}^{\vartheta}},\ k=0,\ldots,K_\ell^u-1. \tag{44}$$

By saying $\frac{P_{\ell,k}}{P_u} \le 1,\ k=0,\ldots,K_\ell^u-1$, we mean the reverse link transmit power must not exceed its maximum value. If $\vartheta = 0$, all UEs have the same transmit power and no power control regime is adopted. When $\vartheta = 1$, the pathloss represented by the pathloss exponent is completely compensated.

IV. FORWARD LINK ANALYSIS

The signal transmitted by the ℓ-th BS is

$$\mathbf{x}_\ell = \sum_{k=0}^{K_\ell^d-1}\sqrt{\frac{P_{\ell,k}}{N_{\mathsf{a}}}}\mathbf{f}_{\ell,k}s_{\ell,k}, \tag{45}$$

$$\overline{\mathsf{den}}_u^{\mathsf{MF}} = \alpha_u^2 N_{\mathsf{a}}\left(1+\sum_\ell\sum_{\mathrm{k}=0}^{K_\ell^u-1}\frac{P_{\ell,\mathrm{k}}}{P_u}\mathsf{SNR}_{\ell,\mathrm{k}}^u\right) + \alpha_u^2 N_{\mathsf{a}}^2\frac{\sum_{\ell\in\mathcal{C}}\left(\frac{P_{\ell,k}}{P_u}\mathsf{SNR}_{\ell,k}^u\right)^2}{1+\frac{P_k}{P_u}\mathsf{SNR}_k^u+\sum_{\ell\in\mathcal{C}}\frac{P_{\ell,k}}{P_u}\mathsf{SNR}_{\ell,k}^u} + \alpha_u^2\alpha_d(1-\alpha_d)K^d N_{\mathsf{a}}^2\mathsf{INR}$$
$$+\alpha_u^2\alpha_d^2 K^d N_{\mathsf{a}}^2\mathsf{INR} + N_{\mathsf{a}}\alpha_u(1-\alpha_u)\left[2\frac{P_k}{P_u}\mathsf{SNR}_k^u + \sum_{\mathrm{k}\neq k}\frac{P_{\mathrm{k}}}{P_u}\mathsf{SNR}_{\mathrm{k}}^u + \sum_{\ell\neq 0}\sum_{\mathrm{k}}\frac{P_{\ell,\mathrm{k}}}{P_u}\mathsf{SNR}_{\ell,\mathrm{k}}^u + \alpha_d N_{\mathsf{a}}\mathsf{INR} + 1\right] \tag{39}$$

$$\overline{\mathsf{sinr}}_k^{\mathsf{MF}} = \frac{\frac{N_{\mathsf{a}}}{1+\frac{P_k}{P_u}\mathsf{SNR}_k^u+\sum_{\ell\in\mathcal{C}}\frac{P_{\ell,k}}{P_u}\mathsf{SNR}_{\ell,k}^u}\left(\frac{P_k}{P_u}\mathsf{SNR}_k^u\right)^2}{1+\sum_\ell\sum_{\mathrm{k}=0}^{K_\ell^u-1}\frac{P_{\ell,\mathrm{k}}}{P_u}\mathsf{SNR}_{\ell,\mathrm{k}}^u + \frac{N_{\mathsf{a}}}{1+\frac{P_k}{P_u}\mathsf{SNR}_k^u+\sum_{\ell\in\mathcal{C}}\frac{P_{\ell,k}}{P_u}\mathsf{SNR}_{\ell,k}^u}\sum_{\ell\in\mathcal{C}}\left(\frac{P_{\ell,k}}{P_u}\mathsf{SNR}_{\ell,k}^u\right)^2} \tag{42}$$

where $P_{\ell,k}$ is the power allocated to the data symbol $s_{\ell,k} \sim \mathcal{N}_{\mathbb{C}}(0,1)$, which is precoded by $\mathbf{f}_{\ell,k}$ and intended for its k-th user. The power allocation satisfies

$$\sum_{k=0}^{K_\ell^d-1} P_{\ell,k} = P_d, \tag{46}$$

where P_d is the forward link power per cell. Since the BS operates in FD mode, the reverse link users are only corrupted by the SI while the forward link users are SI-free. But since the reverse link users users are sending simultaneously when the forward link users users are receiving, the latter are vulnerable to the IUI caused by the reverse link users.

Upon data transmission from the BS of interest, the k-th user observes the following quantized received signal from the BS of interest as

$$\begin{aligned} y_{q,k}^d = \alpha_d \sum_{\ell} \sum_{\mathrm{k}=0}^{K_\ell^d-1} \sqrt{\frac{G_{\ell,k}P_{\ell,\mathrm{k}}}{N_{\mathsf{a}}}}\mathbf{h}_{\ell,k}^* \mathbf{f}_{\ell,\mathrm{k}} s_{\ell,\mathrm{k}} \\ + \sum_{\ell} \sum_{\mathrm{k}=0}^{K_\ell^d-1} \sqrt{\frac{G_{\ell,k}P_{\ell,\mathrm{k}}}{N_{\mathsf{a}}}}\mathbf{h}_{\ell,k}^* \mathbf{q}_{d,\ell} \\ + \sum_{\ell} \sum_{\mathrm{k}=0}^{K_\ell^u-1} \sqrt{T_{(\ell,\mathrm{k}),k}P_{\ell,\mathrm{k}}^u}\mathbf{g}_{(\ell,\mathrm{k}),k} s_{\ell,\mathrm{k}}^u + v_k. \end{aligned} \tag{47}$$

In the reverse link, the LMMSE channel estimates are available at the BSs from the corresponding pilot observations. Therefore, exploiting the channel reciprocity in TDD, we can skip the channel estimation at the UEs. Nevertheless, the channel estimation at the UEs can be carried out by sending precoded forward pilots, using at least one precoded pilot per UE and per coherence time (block of samples).

In the rest of this section, we focus on the analysis of channel-hardening reliant receivers.

A. CHANNEL HARDENING

Since we consider receivers taking advantage of channel hardening, the k-th user served by the BS of interest regards $\mathbb{E}[\mathbf{h}_k^*\mathbf{f}_k]$ as its precoded channel wherein the small-scale fading is averaged. The variation of the actual precoded channel around the mean incurs SI, such that (47) can be formulated as (48) shown at the bottom of the page.

Theorem 5: For channel hardening, the output SQINR of the k-th downlink user is given by (49).

$$\overline{\mathsf{sqinr}}_k = \frac{\alpha_d^2 \frac{P_k}{P_d N_{\mathsf{a}}} \mathsf{SNR}_k^d \left|\mathbb{E}\left[\mathbf{h}_k^*\mathbf{f}_k\right]\right|^2}{\overline{\mathsf{den}}_d} \tag{49}$$

Here, $\overline{\mathsf{den}}_d$ is expressed by (50) shown at the bottom of the page, where $\mathsf{SNR}_{(\ell,\mathrm{k}),k}^{\mathsf{iui}} = P_u T_{(\ell,\mathrm{k}),k}/\sigma^2$.

Proof: The proof is straightforward by evaluating the expected value of the power of each term. The expected value of the power of channel estimation error is nothing but the variance of the precoded channel. The derivation cannot go further because this result is considered for any given BS precoder. Later in Theorem 6, we will specify the BS precoder and hence the derivation will be more intricate. ■

B. MATCHED FILTER PRECODER

The ℓ-th BS gathers channel estimates $\hat{\mathbf{h}}_{\ell,(\ell,0)}, \ldots, \hat{\mathbf{h}}_{\ell,(\ell,K_\ell^d-1)}$ from the reverse link pilots transmitted by its own users. With a matched filter transmitter, the precoders at cell ℓ are given by

$$\mathbf{f}_{\ell,k}^{\mathsf{MF}} = \sqrt{N_{\mathsf{a}}} \frac{\hat{\mathbf{h}}_{\ell,(\ell,k)}}{\sqrt{\mathbb{E}\left[\left\|\hat{\mathbf{h}}_{\ell,(\ell,k)}\right\|^2\right]}}, \quad k = 0, \ldots, K_\ell^d - 1, \tag{51}$$

where the precoders share the same properties as the matched filter receiver indicated by Corollary 2.

$$\begin{aligned} y_{q,k}^d = \underbrace{\alpha_d \sqrt{\frac{G_k P_k}{N_{\mathsf{a}}}} \mathbb{E}\left[\mathbf{h}_k^*\mathbf{f}_k\right] s_k}_{\text{Desired Signal}} + \underbrace{\alpha_d \sqrt{\frac{G_k P_k}{N_{\mathsf{a}}}} \left(\mathbf{h}_k^*\mathbf{f}_k - \mathbb{E}\left[\mathbf{h}_k^*\mathbf{f}_k\right]\right) s_k}_{\text{Channel Estimation Error}} + \underbrace{\alpha_d \sum_{\mathrm{k}\neq k} \sqrt{\frac{G_k P_{\mathrm{k}}}{N_{\mathsf{a}}}} \mathbf{h}_k^*\mathbf{f}_{\mathrm{k}} s_{\mathrm{k}}}_{\text{Intra-Cell Interference}} + \underbrace{\sum_{\ell} \sum_{\mathrm{k}=0}^{K_\ell^d-1} \sqrt{\frac{G_{\ell,k}P_{\ell,\mathrm{k}}}{N_{\mathsf{a}}}} \mathbf{h}_{\ell,k}^* \mathbf{q}_\ell}_{\text{Aggregate AQNM}} \\ + \underbrace{\alpha_d \sum_{\ell\neq 0} \sum_{\mathrm{k}=0}^{K_\ell^d-1} \sqrt{\frac{G_{\ell,k}P_{\ell,\mathrm{k}}}{N_{\mathsf{a}}}} \mathbf{h}_{\ell,k}^* \mathbf{f}_{\ell,\mathrm{k}} s_{\ell,\mathrm{k}}}_{\text{Inter-Cell Interference}} + \underbrace{\sum_{\mathrm{k}\neq k} \sqrt{T_{\mathrm{k},k}P_{\ell,\mathrm{k}}^u} \mathbf{g}_{\mathrm{k},k} s_{\mathrm{k},u}}_{\text{Same Cell Inter-User Interference}} + \underbrace{\sum_{\ell\neq 0} \sum_{\mathrm{k}=0}^{K_\ell^u-1} \sqrt{T_{(\ell,\mathrm{k}),k}P_{\ell,\mathrm{k}}^u} \mathbf{g}_{(\ell,\mathrm{k}),k} s_{\ell,\mathrm{k},u}}_{\text{Other Cells Inter-User Interference}} + \underbrace{v_k}_{\text{Noise}} \end{aligned} \tag{48}$$

$$\begin{aligned} \overline{\mathsf{den}}_d = \alpha_d^2 \frac{P_k}{P_d N_{\mathsf{a}}} \mathsf{SNR}_k^d \mathsf{var}\left[\mathbf{h}_k^*\mathbf{f}_k\right] + \alpha_d^2 \sum_{\mathrm{k}\neq k} \frac{P_{\mathrm{k}}}{P_d N_{\mathsf{a}}} \mathsf{SNR}_k^d \mathbb{E}\left[\left|\mathbf{h}_k^*\mathbf{f}_{\mathrm{k}}\right|^2\right] + \alpha_d^2 \sum_{\ell\neq 0} \sum_{\mathrm{k}=0}^{K_\ell^d-1} \frac{P_{\ell,\mathrm{k}}}{P_d N_{\mathsf{a}}} \mathsf{SNR}_{\ell,k}^d \mathbb{E}\left[\left|\mathbf{h}_{\ell,k}^*\mathbf{f}_{\ell,\mathrm{k}}\right|^2\right] \\ + \sum_{\ell} \sum_{\mathrm{k}=0}^{K_\ell^u-1} \frac{P_{\ell,\mathrm{k}}^u}{P_u} \mathsf{SNR}_{(\ell,\mathrm{k}),k}^{\mathsf{iui}} \mathbb{E}\left[\left|\mathbf{g}_{(\ell,\mathrm{k}),k}\right|^2\right] + \sum_{\ell} \frac{P_{\ell,k}}{P_d N_{\mathsf{a}}} \mathsf{SNR}_{\ell,k}^d \mathbb{E}\left[\left|\mathbf{h}_{\ell,k}^*\mathbf{q}_{d,\ell}\right|^2\right] + 1 \end{aligned} \tag{50}$$

Recall the expression of the reverse link channel estimate at the cell of interest (19), and referring to the analogy with the matched filter receiver, the k-th matched filter precoder at the BS of interest is expressed by

$$\mathbf{f}_k^{\mathsf{MF}} = \sqrt{\frac{\frac{P_k}{P_u}\mathsf{SNR}_k^u}{1+\frac{P_k}{P_u}\mathsf{SNR}_k^u+\sum_{\ell\in\mathcal{C}}\frac{P_{\ell,k}}{P_u}\mathsf{SNR}_{\ell,k}^u}} \times \left(\mathbf{h}_k+\sum_{\ell\in\mathcal{C}}\sqrt{\frac{\frac{P_{\ell,k}}{P_u}\mathsf{SNR}_{\ell,k}^u}{\frac{P_k}{P_u}\mathsf{SNR}_k^u}}\mathbf{h}_{\ell,k}+\mathbf{v}_k'\right). \quad (52)$$

which exactly matches the reverse link matched filter receiver.

Theorem 6: For channel hardening and with a matched filter precoder, the output SQINR of the k-th downlink user is expressed by (53).

$$\overline{\mathsf{sqinr}}_k^{\mathsf{MF}} = \frac{\frac{P_k}{P_u}\mathsf{SNR}_k^u\frac{P_k}{P_d}\mathsf{SNR}_k^d N_{\mathsf{a}}}{\left(1+\frac{P_k}{P_u}\mathsf{SNR}_k^u+\sum_{\ell\in\mathcal{C}}\frac{P_{\ell,k}}{P_u}\mathsf{SNR}_{\ell,k}^u\right)\overline{\mathsf{den}}_d^{\mathsf{MF}}} \quad (53)$$

Remark 4: The fractions $\frac{P_{\ell,k}}{P_u}$ and $\frac{P_{\ell,k}}{P_d}$ for any ℓ and k, are the fractional power control and power allocation coefficients, respectively.

While introducing the new term $\varrho = \mathsf{SNR}_{\ell,(l,k)}^d/\mathsf{SNR}_{\ell,(l,k)}^u$ for any ℓ, l and k as the *forward-reverse signal-to-noise ratio (SNR) ratio*, the output SQINR of the k-th downlink UE becomes

$$\overline{\mathsf{sqinr}}_k^{\mathsf{MF}} = \frac{\alpha_d^2\frac{N_{\mathsf{a}}}{\varrho+\frac{P_k}{P_u}\mathsf{SNR}_k^d+\sum_{\ell\in\mathcal{C}}\frac{P_{\ell,k}}{P_u}\mathsf{SNR}_{\ell,k}^d}\frac{P_k}{P_u}\frac{P_k}{P_d}\left(\mathsf{SNR}_k^d\right)^2}{\overline{\mathsf{den}}_d^{\mathsf{MF}}} \quad (54)$$

where $\overline{\mathsf{den}}_d^{\mathsf{MF}}$ is given by (55), shown at the bottom of the page.

Proof: The proof of Theorem 6 is provided in Appendix E. ■

Proposition 5: Considering a single-cell multiuser system (without any inter-cell interference) with perfect CSI, Corollary 3 entails the results for forward link in [32].

Proposition 6: With channel hardening, without full-duplexing (no IUI), with full-resolution and with a matched filter precoder, the output SINR of the k-th downlink user is given by (56).

Remark 5: Note that Proposition 6 entails the same result for forward link derived in [47].

Neglecting pilot contamination and assuming $\varrho + \frac{P_k}{P_u}\mathsf{SNR}_k^d \approx \frac{P_k}{P_u}\mathsf{SNR}_k^d$, the output SINR of the k-th downlink user (56) is reduced to (57).

$$\overline{\mathsf{sinr}}_k^{\mathsf{MF}} \approx \frac{\frac{P_k}{P_u}\frac{P_k}{P_d}\left(\mathsf{SNR}_k^d\right)^2 N_{\mathsf{a}}}{\left(\varrho+\frac{P_k}{P_u}\mathsf{SNR}_k^d\right)\left(1+\sum_\ell \mathsf{SNR}_{\ell,k}^d\right)}. \quad (57)$$

Remark 6: Note that the output SINR expression (57) admits a duality with its reverse link counterpart (43). In addition, the assumption of $\varrho + \frac{P_k}{P_u}\mathsf{SNR}_k^d \approx \frac{P_k}{P_u}\mathsf{SNR}_k^d$ is equivalent to considering a perfect channel estimation and therefore any achievable SINRs in the reverse link can be also achieved in the forward link if the same total power is transmitted.

C. TRACTABILITY

Finding closed-form expressions of the proposed systems is not tractable. However, under special assumptions, tractable expressions of the CDF as well as the spectral efficiency can be derived.

Proposition 7: Without full-duplexing, with full resolution, without pilot contamination, without noise, and with fixed number of users as well as assuming the number of downlink users (K) is the same in all the cells, the CDF and the average spectral efficiency per user under uniform power allocation scheme satisfy (58) shown at the bottom of the next page, and (59), respectively.

$$\overline{\mathcal{I}}_{\overline{\mathsf{sir}}_k^{\mathsf{MF}}} = \log_2(e)\int_0^{+\infty}\frac{1-e^{-zN_{\mathsf{a}}/K}}{{}_1F_1(1,1-\delta,z)}\frac{dz}{z}, \quad (59)$$

Here, the function $\mathsf{B}_\delta(\cdot)$ is defined by

$$\mathsf{B}_\delta(x) = \frac{{}_2F_1(1,\delta+1;2\delta+2;-1/x)\delta}{x^{1+2\delta}\Gamma(2\delta+2)\Gamma^2(1-\delta)}, \quad (60)$$

Here, ${}_2F_1(\cdot)$ is the Gauss hypergeometric function, ${}_1F_1(\cdot)$ is the confluent hypergeometric or Kumar function, and $\Gamma(\cdot)$ is the Gamma function.

$$\overline{\mathsf{den}}_d^{\mathsf{MF}} = 1+\alpha_d^2\sum_\ell \mathsf{SNR}_{\ell,k}^d + \alpha_d^2\sum_{\ell\in\mathcal{C}}\frac{N_{\mathsf{a}}}{\varrho+\frac{P_k}{P_u}\mathsf{SNR}_{\ell,k}^d+\sum_{l\in\mathcal{C}}\frac{P_{l,k}}{P_u}\mathsf{SNR}_{\ell,(l,k)}^d}\frac{P_k}{P_u}\frac{P_{\ell,k}}{P_d}\left(\mathsf{SNR}_{\ell,k}^d\right)^2 + \sum_\ell\sum_{\mathrm{k}=0}^{K_\ell^u-1}\frac{P_{\ell,\mathrm{k}}^u}{P_u}\mathsf{SNR}_{(\ell,\mathrm{k}),k}^{\mathsf{iui}} + \alpha_d(1-\alpha_d)\sum_\ell\frac{P_{\ell,k}}{P_d}\mathsf{SNR}_{\ell,k}^d\left(K_\ell^d+1\right) \quad (55)$$

$$\overline{\mathsf{sinr}}_k^{\mathsf{MF}} = \frac{\frac{N_{\mathsf{a}}}{\varrho+\frac{P_k}{P_u}\mathsf{SNR}_k^d+\sum_{\ell\in\mathcal{C}}\frac{P_{\ell,k}}{P_u}\mathsf{SNR}_{\ell,k}^d}\frac{P_k}{P_u}\frac{P_k}{P_d}\left(\mathsf{SNR}_k^d\right)^2}{1+\alpha_d^2\sum_\ell \mathsf{SNR}_{\ell,k}^d+\alpha_d^2\sum_{\ell\in\mathcal{C}}\frac{N_{\mathsf{a}}}{\varrho+\frac{P_k}{P_u}\mathsf{SNR}_{\ell,k}^d+\sum_{l\in\mathcal{C}}\frac{P_{l,k}}{P_u}\mathsf{SNR}_{\ell,(l,k)}^d}\frac{P_k}{P_u}\frac{P_{\ell,k}}{P_d}\left(\mathsf{SNR}_{\ell,k}^d\right)^2} \quad (56)$$

TABLE 3. Values for parameter s for typical pathloss exponents η [57, Table 10.1].

η	s
3.5	-0.672
3.6	-0.71
3.7	-0.747
3.8	-0.783
3.9	-0.819
4.0	-0.854

In (58), the term $s^* < 0$ is defined as the solution of

$$s^{*\delta}\gamma\left(-\delta, s^*\right) = 0. \tag{61}$$

where $\gamma(\cdot,\cdot)$ is the incomplete lower Gamma function and $\delta = 2/\eta$. We solve (61) to find s* which then determines the values of η and δ in this tractable case. Common values of the parameter s^* for typical pathloss exponents are given by Table 3.

Proof: The proof of the results entailed by Proposition 7 are derived in [47]. ■

V. ASYMPTOTIC ANALYSIS AND POWER SCALING LAWS

In the section, we investigate the effects of the number of quantization bits, number of BS antennas, number of users, and BS and UE power budgets on spectral efficiency for the reverse and forward links. In the next Section, we carry out the analysis for the channel hardening case.

Lemma 3: For a fixed power budget, fixed number of transmit antennas and full-resolution ($b \to \infty$, $\alpha_u = \alpha_d = 1$), the spectral efficiencies for reverse and forward links converge to (62) and (63), shown at the bottom of the page, shown at the bottom of the page, respectively.

In (62) and (63), the quantization error introduced by finite resolution ADCs and DACs vanishes for full-resolution. When the number of antennas is fixed, spectral efficiency for uplink/downlink users becomes constant. Although increasing ADC/DAC resolution can improve the uplink/downlink spectral efficiency, the latter is limited by pilot contamination, SI, IUI and cellular interference including intra and inter-cell interference.

Lemma 4: For a fixed number of antennas N_{a} and a fixed number of bits b as well as assuming uniform power allocation for the forward link, when $\mathsf{SNR}_k^u, \mathsf{SNR}_k^d \to \infty$, the spectral efficiency for the reverse and forward links converge to

$$\frac{\bar{\mathcal{I}}_u^{\mathsf{MF}}}{B} \to \log\left(1 + \frac{N_{\mathsf{a}}}{\alpha_u(2-\alpha_u)}\right) \tag{64}$$

$$\frac{\bar{\mathcal{I}}_d^{\mathsf{MF}}}{B} \to \log\left(1 + \frac{\alpha_d N_{\mathsf{a}}}{K^d - \alpha_d + 1}\right). \tag{65}$$

In (64) and (65), the spectral efficiency for the reverse and forward links depend on the number of antennas N_{a}, number of users K, and the AQNM ADC/DAC resolution parameter α. When the transmit power at the BS and UE in the cell of interest grows large enough, the aggregate interference as well as the pilot contamination are eliminated.

Lemma 5: If the transmit powers of the BS and each user are scaled with the number of antennas N_{a}, i.e., $P = \frac{E}{N_{\mathsf{a}}}$ where E is fixed, as $N_{\mathsf{a}} \to \infty$, the spectral efficiencies for reverse and forward links converge to

$$\frac{\bar{\mathcal{I}}_u^{\mathsf{MF}}}{B} \to \log\left(1 + \frac{\alpha_u\left(\frac{E_k}{E_u}\mathsf{SNR}_k^u\right)^2}{1 + \alpha_d\left(\alpha_u K^d + 1 - \alpha_u\right)\mathsf{INR}}\right) \tag{66}$$

$$\begin{cases} F_{\overline{\mathsf{sir}}_k^{\mathsf{MF}}}(\tau) \cong e^{s^*\left(\frac{N_{\mathsf{a}}}{\tau K}-1\right)} & 0 \le \tau < \frac{N_{\mathsf{a}}/K}{3+\varepsilon} \\ F_{\overline{\mathsf{sir}}_k^{\mathsf{MF}}}(\tau) = 1 - \left(\frac{N_{\mathsf{a}}}{\tau K} - 1\right)^{\delta}\mathsf{sinc}(\delta) + \mathsf{B}_{\delta}\left(\frac{\tau K}{N_{\mathsf{a}}-2\tau K}\right) & \frac{N_{\mathsf{a}}/K}{3} \le \tau < \frac{N_{\mathsf{a}}/K}{2} \\ F_{\overline{\mathsf{sir}}_k^{\mathsf{MF}}}(\tau) = 1 - \left(\frac{N_{\mathsf{a}}}{\tau K} - 1\right)^{\delta}\mathsf{sinc}(\delta) & \frac{N_{\mathsf{a}}/K}{2} \le \tau < \frac{N_{\mathsf{a}}}{K} \end{cases} \tag{58}$$

$$\frac{\bar{\mathcal{I}}_u^{\mathsf{MF}}}{B} \to \log\left(1 + \frac{\frac{\left(\frac{P_k}{P_u}\mathsf{SNR}_k^u\right)^2 N_{\mathsf{a}}}{1+\frac{P_k}{P_u}\mathsf{SNR}_k^u + \sum_{\ell\in\mathcal{C}}\frac{P_{\ell,k}}{P_u}\mathsf{SNR}_{\ell,k}^u}}{1 + \sum_{\ell}\sum_{\mathrm{k}=0}^{K_\ell^u-1}\frac{P_{\ell,\mathrm{k}}}{P_u}\mathsf{SNR}_{\ell,\mathrm{k}}^u + N_{\mathsf{a}}\frac{\sum_{\ell\in\mathcal{C}}\left(\frac{P_{\ell,k}}{P_u}\mathsf{SNR}_{\ell,k}^u\right)^2}{1+\frac{P_k}{P_u}\mathsf{SNR}_k^u + \sum_{\ell\in\mathcal{C}}\frac{P_{\ell,k}}{P_u}\mathsf{SNR}_{\ell,k}^u} + N_{\mathsf{a}}K^d\mathsf{INR}}\right) \tag{62}$$

$$\frac{\bar{\mathcal{I}}_d^{\mathsf{MF}}}{B} \to \log\left(1 + \frac{\frac{N_{\mathsf{a}}}{\varrho + \frac{P_k}{P_u}\mathsf{SNR}_k^d + \sum_{\ell\in\mathcal{C}}\frac{P_{\ell,k}}{P_u}\mathsf{SNR}_{\ell,k}^d}\frac{P_k}{P_u}\frac{P_k}{P_d}\left(\mathsf{SNR}_k^d\right)^2}{1 + \sum_{\ell}\mathsf{SNR}_{\ell,k}^d + \sum_{\ell\in\mathcal{C}}\frac{N_{\mathsf{a}}}{\varrho + \frac{P_k}{P_u}\mathsf{SNR}_{\ell,k}^d + \sum_{l\in\mathcal{C}}\frac{P_{l,k}}{P_u}\mathsf{SNR}_{\ell,(l,k)}^d}\frac{P_k}{P_u}\frac{P_{\ell,k}}{P_d}\left(\mathsf{SNR}_{\ell,k}^d\right)^2 + \sum_{\ell}\sum_{\mathrm{k}=0}^{K_\ell^u-1}\frac{P_{\ell,\mathrm{k}}^u}{P_u}\mathsf{SNR}_{(\ell,\mathrm{k}),k}^{\mathsf{iui}}}\right) \tag{63}$$

$$\frac{\bar{\mathcal{I}}_d^{\mathsf{MF}}}{B} \to \log\left(1+\frac{\alpha_d^2}{\varrho}\frac{E_k}{E_u}\frac{E_k}{E_d}\left(\mathsf{SNR}_k^d\right)^2\right). \tag{67}$$

In (66) and (67), we found that using a proper power scaling law and more antennas can eliminate the inter-user, inter-cell and intra-cell interference as well as pilot contamination and noise for both the reverse and forward links. However, the reverse link is still corrupted by the SI.

Lemma 6: If the transmit power and number of users per cell are fixed, the spectral efficiencies for reverse and forward links as $N_{\mathsf{a}}/K \to \infty$ converge to (68) and (69), respectively.

Equations (68) and (69) corroborate the fact that increasing the ratio (N_{a}/K) leads to pilot contamination dominance which imposes a limit on the SQINR. The reverse link performance is also saturated by the SI in addition to the pilot contamination.

VI. EXTENSION TO MILLIMETER WAVE BANDS

Up to this point, we have been focusing on sub-7 GHz LTE bands. In this section, we provide an extension of the previous analysis to the mmWave spectrum from 30 to 300 GHz[5] whereas most users operate at a carrier frequency below 7 GHz. The major benefits of operating in mmWave frequencies is the availability of larger bandwidths and unlicensed spectrum. For example, channels with 2 GHz of bandwidth are common for systems operating at 60 GHz unlicensed mmWave bands. Larger bandwidth channels mean higher data rates.

A. CHANNEL MODEL

Radio channel properties depend on the carrier frequency. Electromagnetic waves propagating at low/medium frequency can travel for long distances due to low penetration loss, small pathloss, and rich scattering paths. A good channel model to describe such a phenomenon is the Complex Gaussian or Rayleigh fading. For mmWave bands, electromagnetic waves travel short ranges due to high penetration loss, large pathloss, and limited scattering paths. In other words, mmWave channels are generally sparse wherein the number of rays is small and grouped in a small clusters. A good common channel model that can capture these properties is the 3D geometric channel, a.k.a. the *Saleh-Valenzuela* model, expressed as

$$\mathbf{H} = \sqrt{\frac{N_{\mathsf{RX}}N_{\mathsf{TX}}}{CR_c}}\sum_{c=0}^{C-1}\sum_{r_c=0}^{R_c-1}\alpha_{r_c}\mathbf{a}_{\mathsf{RX}}(\theta_{r_c})\mathbf{a}_{\mathsf{TX}}^*(\phi_{r_c}), \tag{70}$$

where N_{RX} and N_{TX} are the numbers of antennas at RX and TX, respectively. C is the number of clusters, R_c is the number of rays per cluster, and θ_{r_c} and ϕ_{r_c} are the angles of arrival (AoA) and departure (AoD) of the r_c-th ray, respectively. Each ray has a complex path gain α_{r_c}. Also, $\mathbf{a}_{\mathsf{RX}}(\theta)$ and $\mathbf{a}_{\mathsf{TX}}(\phi)$ are the RX and TX antenna array response vectors, respectively. We adopt a uniform linear array (ULA) wherein the array response vector is given by

$$\mathbf{a}_{\mathsf{RX}}(\theta) = \frac{1}{\sqrt{N_{\mathsf{RX}}}}\left[1, \mathrm{e}^{i\frac{2\pi r}{\lambda}\sin(\theta)}, \ldots, \mathrm{e}^{i\frac{2\pi r}{\lambda}(N_{\mathsf{RX}}-1)\sin(\theta)}\right]^T. \tag{71}$$

where r and λ are the antenna spacing and signal wavelength, respectively.

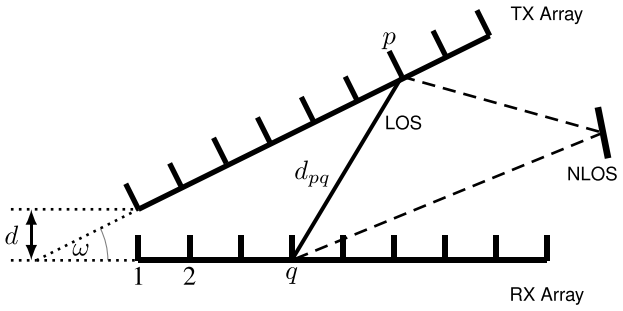

FIGURE 5. Relative position of TX and RX arrays at BS. Given that the TX and RX arrays are collocated, the far-field assumption that the signal impinges on the antenna array as a planar wave does not hold. Instead, for FD transceivers, it is more suitable to assume that the signal impinges on the array as a spherical wave for the near-field LOS channel.

B. SELF-INTERFERENCE CHANNEL MODEL

Per Fig. 5, the SI leakage at the BS is modeled by the channel matrix $\mathbf{H}_{\mathsf{S}}$. The separation, or transceiver gap, between TX

5. Although a rigorous definition of mmWave frequencies would place them between 30 and 300 GHz, industry has loosely defined them to include the spectrum from 10 to 300 GHz.

$$\frac{\bar{\mathcal{I}}_u^{\mathsf{MF}}}{B} \to \log\left(1+\frac{\alpha_u\left(\frac{P_k}{P_u}\mathsf{SNR}_k^u\right)^2}{\alpha_u\frac{\sum_{\ell\in\mathcal{C}}\left(\frac{P_{\ell,k}}{P_u}\mathsf{SNR}_{\ell,k}^u\right)^2}{1+\frac{P_k}{P_u}\mathsf{SNR}_k^u+\sum_{\ell\in\mathcal{C}}\frac{P_{\ell,k}}{P_u}\mathsf{SNR}_{\ell,k}^u}+\alpha_d\left(\alpha_u K^d+1-\alpha_u\right)\mathsf{INR}}\right) \tag{68}$$

$$\frac{\bar{\mathcal{I}}_d^{\mathsf{MF}}}{B} \to \log\left(1+\frac{\frac{1}{\varrho+\frac{P_k}{P_u}\mathsf{SNR}_k^d+\sum_{\ell\in\mathcal{C}}\frac{P_{\ell,k}}{P_u}\mathsf{SNR}_{\ell,k}^d}\frac{P_k}{P_u}\frac{P_k}{P_d}\left(\mathsf{SNR}_k^d\right)^2}{\sum_{\ell\in\mathcal{C}}\frac{1}{\varrho+\frac{P_k}{P_u}\mathsf{SNR}_{\ell,k}^d+\sum_{l\in\mathcal{C}}\frac{P_{l,k}}{P_u}\mathsf{SNR}_{\ell,(l,k)}^d}\frac{P_k}{P_u}\frac{P_{\ell,k}}{P_d}\left(\mathsf{SNR}_{\ell,k}^d\right)^2}\right) \tag{69}$$

and RX arrays is defined by distance d while the transceiver incline is determined by ω. The SI channel is decomposed into a static line-of-sight (LOS) channel modeled by $\mathbf{H}_{\mathsf{LOS}}$, which is derived from the geometry of the transceiver, and a non-line-of-sight (NLOS) channel described by $\mathbf{H}_{\mathsf{NLOS}}$ which follows the geometric channel model defined by (70). The (q, p)-th entry of the LOS SI leakage matrix can be written as

$$\left[\mathbf{H}_{\mathsf{LOS}}\right]_{qp} = \frac{1}{d_{pq}} \mathrm{e}^{-i2\pi \frac{d_{pq}}{\lambda}}, \tag{72}$$

where d_{pq} is the distance between the p-th antenna in the TX array and q-th antenna in the RX array at BS given by (74) shown at the bottom of the page. The aggregate SI channel matrix can be obtained by

$$\mathbf{H}_{\mathsf{S}} = \underbrace{\sqrt{\frac{\kappa}{\kappa+1}}\mathbf{H}_{\mathsf{LOS}}}_{\text{Near-Field}} + \underbrace{\sqrt{\frac{1}{\kappa+1}}\mathbf{H}_{\mathsf{NLOS}}}_{\text{Far-Field}}, \tag{73}$$

where κ is the Rician factor.

C. SIGNAL PROCESSING PERSPECTIVE

Communicating at mmWave bands is not simply a matter of just switching the frequency band to be higher. Migrating to mmWave completely changes the assumptions that underlie prior developments in signal processing for communications. The RF hardware introduces constraints that have significant effects on the beamforming, precoding, power consumption, etc. Unlike universal mobile telecommunications system (UMTS) and long term evolution (LTE), devices operating at mmWave frequencies are power hungry; e.g., the ADC/DAC consumes hefty power because higher sampling rates are needed for the larger bandwidths in mmWave communications.

Adopting a full-digital architecture for the large antenna arrays needed for mmWave LTE communications becomes impractical. In fact, for the full-digital architecture, an RF chain is dedicated for each antenna, but due to the higher power consumption of each RF chain at mmWave bands, the full-digital solution for mmWave communications is not feasible. To reduce the power consumption, adopting a hybrid analog/digital architecture, wherein the number of RF chains is reduced and each RF chain is connected to the entire array of antennas as illustrated by Fig. 9, may solve this shortcoming. Although such a solution reduces the number of RF chains and hence sacrifices degrees of freedom leading to reduction in spectral efficiency, the reduction in the total power consumption can lead to a practical implementation. For comparison, the full-digital architecture of the FD BS is illustrated by Fig. 4 and the hybrid analog/digital architecture of the FD BS by Fig. 6.

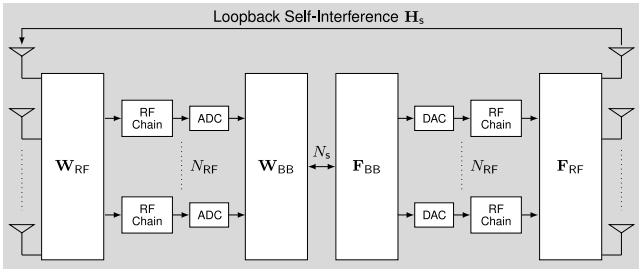

FIGURE 6. Basic abstraction of the hybrid analog/digital architecture of the FD BS. $\mathbf{W}_{\mathsf{RF}}$ and $\mathbf{W}_{\mathsf{BB}}$ are the analog and digital combiners at the BS, respectively. $\mathbf{F}_{\mathsf{RF}}$ and $\mathbf{F}_{\mathsf{BB}}$ are the analog and digital precoders at the BS, respectively. The number of streams that the BS can sustain is denoted by N_{S} while the number of RF chains is denoted by N_{RF}. We further illustrate the loopback SI from the transmit to receive arrays of the BS and we denote by $\mathbf{H}_{\mathsf{S}}$ the aggregated SI channel.

The full-digital precoder or combiner designed in the previous sections for the reverse and forward links is neither energy-efficient nor feasible for mmWave; however, the designs may serve as benchmarking tools to measure the efficacy of the hybrid beamforming design in Fig. 6. In proceeding with mmWave analysis, we decompose the full-digital solution into the equivalent analog and digital components. Without loss of generality, we conduct the analysis for a given optimal full-digital precoder denoted by $\mathbf{F}_{\mathsf{opt}}$.

In this subsection, we aim at decomposing the optimal precoder $\mathbf{F}_{\mathsf{opt}}$ into the equivalent digital $\mathbf{F}_{\mathsf{BB}}$ and analog $\mathbf{F}_{\mathsf{RF}}$ solutions. The hybrid analog/digital decomposition problem $\mathscr{P}_1$ can be stated as

$$\begin{aligned} \mathscr{P}_1 : \min_{\mathbf{F}_{\mathsf{BB}}, \mathbf{F}_{\mathsf{RF}}} \quad & \|\mathbf{F}_{\mathsf{opt}} - \mathbf{F}_{\mathsf{RF}}\mathbf{F}_{\mathsf{BB}}\|_F^2 \\ \text{s.t.} \quad & \mathbf{F}_{\mathsf{RF}} \in \mathcal{F}_{\mathsf{RF}} \\ & \|\mathbf{F}_{\mathsf{RF}}\mathbf{F}_{\mathsf{BB}}\|_F^2 = N_{\mathsf{s}}, \end{aligned} \tag{75}$$

where $\mathcal{F}_{\mathsf{RF}}$ is the set of feasible RF precoders which correspond to a hybrid architecture based on phase shifters, i.e., the set of matrices with constant-magnitude entries.

D. IMPLEMENTATION OF MILLIMETER WAVE SOLUTIONS

The main objective of this subsection is to illustrate the implementation of the mmWave hybrid analog/digital solutions following these steps:

1) Find full-digital combiner $\mathbf{W} = [\mathbf{w}_0, \mathbf{w}_1, \ldots, \mathbf{w}_{K^u-1}]$ and precoder $\mathbf{F} = [\mathbf{f}_0, \mathbf{f}_1, \ldots, \mathbf{f}_{K^d-1}]$ at the FD BS of interest. Such solutions could be the matched filter as proposed for LTE bands or other solutions such as ZF or MMSE.
2) Decompose full-digital combiner and precoder at the FD BS into the equivalent analog and digital solutions as $\mathbf{W} = \mathbf{W}_{\mathsf{RF}}\mathbf{W}_{\mathsf{BB}}$ and $\mathbf{F} = \mathbf{F}_{\mathsf{RF}}\mathbf{F}_{\mathsf{BB}}$.

$$d_{pq} = \sqrt{\left(\frac{d}{\tan(\omega)} + (q-1)\frac{\lambda}{2}\right)^2 + \left(\frac{d}{\sin(\omega)} + (p-1)\frac{\lambda}{2}\right)^2 - 2\left(\frac{d}{\tan(\omega)} + (q-1)\frac{\lambda}{2}\right)\left(\frac{d}{\sin(\omega)} + (p-1)\frac{\lambda}{2}\right)\cos(\omega)} \tag{74}$$

For the forward link, each user receives a single spatial stream from the BS and hence we assume that the total number of allowable spatial streams is $N_{\mathsf{s}} = K$. In addition, we assume that the maximum number of served users is equal to the number of RF chains at the BS, i.e., $K \leq N_{\mathsf{RF}}$. This is motivated by the spatial multiplexing gain of the proposed multiuser MIMO (MU-MIMO) hybrid precoding system, which is restricted by $\min(N_{\mathsf{RF}}, K)$ for $N_{\mathsf{a}} > N_{\mathsf{RF}}$. For simplicity, the BS uses K out of the N_{RF} available RF chains to serve the K users. In the digital domain, the BS applies a $K \times K$ digital precoder $\mathbf{F}_{\mathsf{BB}}$ followed by an $N_{\mathsf{a}} \times N_{\mathsf{RF}}$ analog precoder $\mathbf{F}_{\mathsf{RF}}$. Since the analog precoder is implemented using analog phase shifters, it has the constant amplitude constraint, i.e., $|[\mathbf{F}_{\mathsf{RF}}]_{m,n}|^2 = \frac{1}{N_{\mathsf{a}}}$. Further, we assume that the angles of the analog phase shifters are quantized and have a finite set of possible values. With these assumptions, the analog precoder entries takes the following form $[\mathbf{F}_{\mathsf{RF}}]_{mn} = \frac{1}{\sqrt{N_{\mathsf{a}}}} e^{i\theta_{mn}}$ where θ_{mn} is the quantized angle at the (m, n)-th entry of the analog precoder. The total power is constrained by normalizing the digital precoder such that $\|\mathbf{F}_{\mathsf{RF}}\mathbf{F}_{\mathsf{BB}}\|_F^2 = N_{\mathsf{s}}$.

For the reverse link, we adopt the same assumptions in terms of the number of spatial streams and RF chains as the forward link. To process the received spatial streams of each user, the BS applies an $N_{\mathsf{a}} \times N_{\mathsf{RF}}$ analog combiner $\mathbf{W}_{\mathsf{RF}}$ followed by a $K \times K$ digital combiner $\mathbf{W}_{\mathsf{BB}}$. Like the analog precoder, the analog combiner is implemented using analog phase shifters and satisfies $|[\mathbf{W}_{\mathsf{RF}}]_{m,n}|^2 = \frac{1}{N_{\mathsf{a}}}$. Given that the analog phase shifters are quantized and have finite set of feasible values, the analog combiner entries satisfies $[\mathbf{W}_{\mathsf{RF}}]_{mn} = \frac{1}{\sqrt{N_{\mathsf{a}}}} e^{i\phi_{mn}}$ where ϕ_{mn} is the quantized angle at the (m, n)-th entry of the analog combiner.

We start by designing the digital precoder $\mathbf{F}_{\mathsf{BB}}$ by using the Least Square (LS) routine as

$$\mathbf{F}_{\mathsf{BB}} = \mathbf{F}_{\mathsf{RF}}^{\dagger}\mathbf{F}_{\mathsf{opt}}, \tag{76}$$

To satisfy the power constraint in (75), we normalize the digital precoder $\mathbf{F}_{\mathsf{BB}}$ by a factor of $\frac{N_{\mathsf{s}}}{\|\mathbf{F}_{\mathsf{RF}}\mathbf{F}_{\mathsf{BB}}\|_F}$.

To design the analog precoder $\mathbf{F}_{\mathsf{RF}}$, we proceed by alternating optimization; i.e., we fix the digital precoder $\mathbf{F}_{\mathsf{BB}}$ and seek the analog precoder that optimizes the following problem

$$\begin{aligned} \mathscr{P}_2 : \min_{\mathbf{F}_{\mathsf{BB}}, \mathbf{F}_{\mathsf{RF}}} \quad & \|\mathbf{F}_{\mathsf{opt}} - \mathbf{F}_{\mathsf{RF}}\mathbf{F}_{\mathsf{BB}}\|_F^2 \\ \text{s.t.} \quad & \mathbf{F}_{\mathsf{RF}} \in \mathcal{F}_{\mathsf{RF}}. \end{aligned} \tag{77}$$

It is important to note that decomposing the optimal solution into a hybrid analog/digital solution is not straightforward due to the non-convex unit modulus constraints. There is no general method to optimally solve (77). To solve this problem, we adopt the approach used by [60] to offer a near-optimal solution of (77). The authors apply the Conjugate Gradient Algorithm for analog precoding based on Manifold Optimization [60]. More details about Manifold Optimization can be found in [61]. The hybrid precoding design is summarized by Algorithm 1.

Algorithm 1 Hybrid Beamforming Design

1: **Input** $\mathbf{F}_{\mathsf{opt}}$
2: Construct $\mathbf{F}_{\mathsf{RF}}^{(0)}$ with random phases and set $n = 0$
3: **repeat**
4: Fix $\mathbf{F}_{\mathsf{RF}}^{(n)}$ and $\mathbf{F}_{\mathsf{BB}}^{(n)} = \mathbf{F}_{\mathsf{RF}}^{(n)\dagger}\mathbf{F}_{\mathsf{opt}}$ Optimize $\mathbf{F}_{\mathsf{RF}}^{(n+1)}$ using [60, Algorithm 1] when $\mathbf{F}_{\mathsf{BB}}^{(n)}$ is fixed.
5: $n \leftarrow n + 1$.
6: **until** a stopping criterion triggers
7: For the digital precoder at the transmit side, normalize $\mathbf{F}_{\mathsf{BB}} \leftarrow \frac{\sqrt{N_{\mathsf{s}}}}{\|\mathbf{F}_{\mathsf{RF}}\mathbf{F}_{\mathsf{BB}}\|_F}\mathbf{F}_{\mathsf{BB}}$

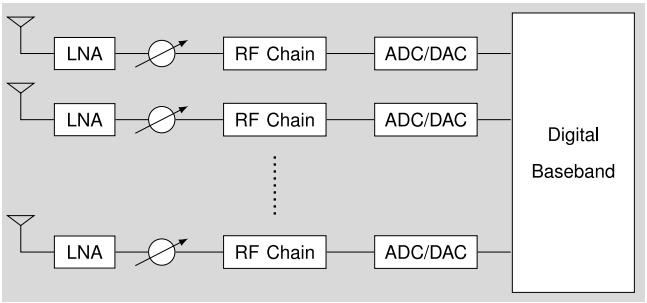

FIGURE 7. Basic abstraction of a digital combiner.

E. UPPER BOUND ON SPECTRAL EFFICIENCY

For the interference-free case, the optimal beamformers diagonalize the channel. By applying the singular value decomposition (SVD) on the channel, we retrieve the singular values and extract the first N_{s} modes associated with the spatial streams. The upper bound for uplink or downlink is given by

$$\mathcal{I}_{\mathsf{Bound}} = \sum_{\ell=0}^{N_{\mathsf{s}}-1} \log\Big(1 + \sigma_\ell(\mathbf{H})^2 \mathsf{SNR}\Big). \tag{78}$$

VII. ENERGY EFFICIENCY AND OUTAGE PROBABILITY

A. ENERGY EFFICIENCY

The energy efficiency, expressed in bits/s/Watt or bits/Joule, is defined as the ratio between the spectral efficiency $\mathcal{I}(\mathsf{sqinr})$ and total power consumption ρ_{Total}. It is expressed as

$$\mathcal{J}(\mathsf{sqinr}) = \frac{\mathcal{I}(\mathsf{sqinr})}{\rho_{\mathsf{Total}}}. \tag{79}$$

In this work, we define the energy efficiency with respect to reverse link since the receiver (BS) is equipped with multiple antennas. For full-digital BS combiner as illustrated by Fig. 7, the total power consumption model is defined by

$$\rho_{\mathsf{Total}}^{\mathsf{DC}} = N_{\mathsf{a}}(\rho_{\mathsf{LNA}} + \rho_{\mathsf{RF}} + 2\rho_{\mathsf{ADC}}), \tag{80}$$

where ρ_{RF} is the power consumption per RF chain which is defined by

$$\rho_{\mathsf{RF}} = \rho_{\mathsf{M}} + \rho_{\mathsf{LO}} + \rho_{\mathsf{LPF}} + \rho_{\mathsf{BB}_{\mathsf{amp}}}. \tag{81}$$

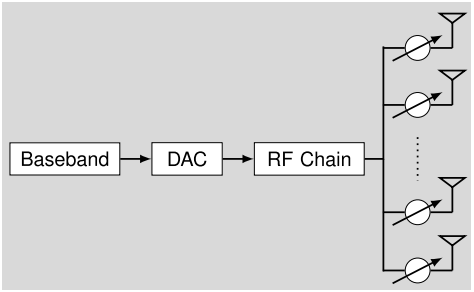

FIGURE 8. Basic abstraction of an analog precoder.

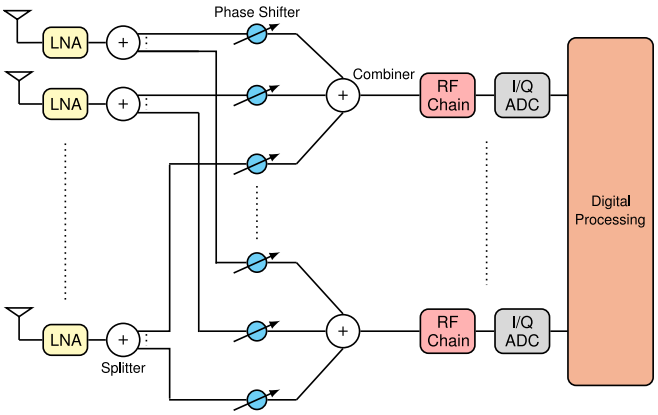

FIGURE 9. Basic abstraction of a hybrid analog/digital combiner.

For analog architecture as illustrated by Fig. 8, the total power consumption can be expressed as

$$\rho_{\text{Total}}^{\text{AC}} = N_{\text{a}}(\rho_{\text{LNA}} + \rho_{\text{PS}}) + \rho_{\text{RF}} + \rho_{\text{C}} + 2\rho_{\text{ADC}}. \quad (82)$$

For hybrid analog/digital architecture as illustrated by Fig. 9, the total power consumption by the mmWave hybrid receiver is expressed by

$$\rho_{\text{Total}}^{\text{HC}} = N_{\text{a}}(\rho_{\text{LNA}} + \rho_{\text{SP}} + N_{\text{RF}}\rho_{\text{PS}}) + N_{\text{RF}}(\rho_{\text{RF}} + \rho_{\text{C}} + 2\rho_{\text{ADC}}). \quad (83)$$

Examples of the power consumption of each device is presented in Table 5. The power consumption of all components except the ADC is independent of the bandwidth B and number of bits b, whereas ρ_{ADC} grows exponentially with b and linearly with B and with Walden's figure of merit for ADCs c, which is the energy consumption per conversion step per Hz. Common values of c are given in Table 6.

In this paper, we selected three reasonable component power consumption models that we approximately identify with current and future generations of technology. The Walden figures of merit c for these ADCs are detailed in Table 6.

- The High Power ADC (HPADC) model is based on an existing device that supports sampling at Gs/s and has been cited in related literature such as [53]. In order to give phase shifters appropriate power consumption values, we pair the existing ADC model with an existing phase shifter model with $\rho_{\text{ADC}} = 2\text{mW}$ in [65].

TABLE 4. System parameters [12], [32], [47], [62].

Parameter	Symbol	Default Value
Bandwidth (LTE)	B	20 MHz
Base station antenna gain		30 dB
Fraction of pilot overhead	β	0.5
Distance between adjacent hexagonal cells		$\sqrt{3}$ km
Fractional frequency reuse	Δ	1
Length of cell side	D_{cell}	1 km
Pathloss exponent	η	4
Pathloss offset		-128 dB
Number of forward/reverse link users per cell	K_ℓ	10
BS density	λ_{BS}	0.1 BS/km^2
UE density	λ_{UE}	0.5 UE/km^2
Number of antennas	N_{a}	100
Number of fading coherence tiles	N_{c}	20,000 (Pedestrians)
Number of pilots per cell	N_{p}	$3K_\ell$
Noise figure		3 dB
Forward link transmit power		40 W
SI channel power	μ_{SI}	10 dB
SI power	P_{SI}	40 W
Reverse link transmit power		200 mW
Shadowing	σ_{dB}	8 dB
Thermal noise spectral density		-174 dBm/Hz
Reverse fractional power control	ϑ	0.7
Forward power allocation	ϑ	0.0 (uniform)
Carrier frequency (mmWave)		28 GHz
Bandwidth (mmWave)		850 MHz
Number of clusters	C	6
Number of rays per cluster	R	8
AoA/AoD angular spread		20°
Transceivers gap	d	2λ
Transceivers incline	ω	$\frac{\pi}{6}$
Rician factor	κ	5 dB

TABLE 5. Power consumption of each device [63].

Device	Notation	Value
Low Noise Amplifier (LNA) [64]	ρ_{LNA}	39 mW
Splitter	ρ_{SP}	19.5 mW
Combiner [65]	ρ_{C}	19.5 mW
Phase Shifter [65], [66]	ρ_{PS}	2 mW
Mixer [67]	ρ_{M}	16.8 mW
Local Oscillator [68]	ρ_{LO}	5 mW
Low Pass Filter [68]	ρ_{LPF}	14 mW
Baseband Amplifier [68]	$\rho_{\text{BB}_{\text{amp}}}$	5 mW
ADC	ρ_{ADC}	$cB2^b$

TABLE 6. ADC power consumption per sample per level, c [63].

Scenario	Value	Generation
LPADC	5 fJ/step/Hz	Low power (ideal future value)
IPADC	65 fJ/step/Hz	Intermediate Power
HPADC	494 fJ/step/Hz	High power (State of the art)

- The Low Power ADC (LPADC) model considers a likely future best-case scenario deduced from the hardware survey [31]. Likewise, we pair this "best case scenario" with a best case phase shifter model, with negligible power consumption $\sim 0\text{mW}$ in [66].
- The ADC power values are rapidly changing, and we consider the extreme cases of well-established HPADC [53] and future LPADC [31]. Very recently a new Intermediate Power ADC (IPADC) has been proposed in [69]. Given this dynamic situation, we complement our study by using the method and associated Web visualization tool in [70] to enable researchers include advances in ADC technology.

B. OUTAGE PROBABILITY

Once a transmission strategy is specified, the corresponding CDF or outage probability for rate R (bits/s/Hz) is then

$$P_{\text{out}}(\text{sqinr}, R) = \mathbb{P}\big[\mathcal{I}(\text{sqinr}) < R\big], \quad (84)$$

With available powerful channel codes, the probability of error when there is no outage is very small and hence the outage probability is an accurate approximation for the actual block error probability [71]. As justified in the literature, radio systems such as UMTS and LTE operate at a target error probability [71]. Therefore, the primary communications performance measure is the maximum rate,[6] at each sqinr, such that this threshold ϵ is not overtaken, i.e.,

$$R_\epsilon(\text{sqinr}) = \max_{\zeta}\{\zeta : P_{\text{out}}(\text{sqinr}, \zeta) \leq \epsilon\}. \tag{85}$$

VIII. NUMERICAL RESULTS

In this section, we discuss numerical results of the system performance. Unless otherwise stated, Table 4 presents the values of the system parameters.[7] We assume uniform power allocation for the forward links as well as a two-tier hexagonal network.

For hexagonal and square grids, we draw the geometry of the cells wherein a BS is dropped at the center of each cell (square or hexagonal) and users are uniformly distributed in each cell. For PPP tessellations, we draw the Voronoi network wherein a BS is dropped in each Voronoi cell and the BS locations are generated using PPP with rate λ_{BS} while user locations are generated using PPP with rate λ_{UE}.

The comparison of the analytical solution stated by Proposition 7 with the simulation-based results is illustrated by Fig. 10. The gap between the analytical results (which are asymptotic in the shadowing standard deviation and number of cells) and simulation results (with only 19 hexagonal and 25 square grid cells) is always less than 2 dB. As the strength of the shadowing and number of cells increases, the gap shrinks as the simulation curves converge to their analytical counterparts. Likewise, if the BS locations cease to conform to a lattice and adopt a more irregular layout, the simulation curves would shift left of the analytical ones based on a regular layout.

Fig. 11 illustrates the CDF of the average reverse link SQINR. When the number of downlink users is large (20 users per cell) and hence there is significant SI power, the CDF performance worsens, and vice-versa. In addition, by increasing the ratio N_{a}/K_ℓ, the user beams become exceedingly narrow which allows the desired signal to dominate the noise and rejects a large amount of interference. In addition, by increasing the SI channel power from 10 to 15 dB, the SI power increases and hence the CDF worsens. Furthermore, antenna array directivity plays an important role in compensating pathloss and suppressing interference.

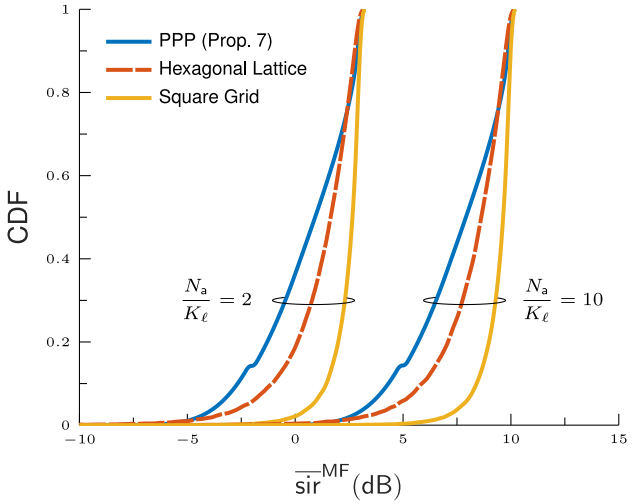

FIGURE 10. Forward link results: Large-scale distributions of $\overline{\text{sir}}^{\text{MF}}$ of an interference-limited network with uniform power allocation, where the number of pilots per cell $N_{\text{P}} \longrightarrow \infty$. Comparison between the analytical solution in Proposition 7 and the simulation-based results for a hexagonal with 2-tier (19 cells) and a square (25 cells) lattice networks.

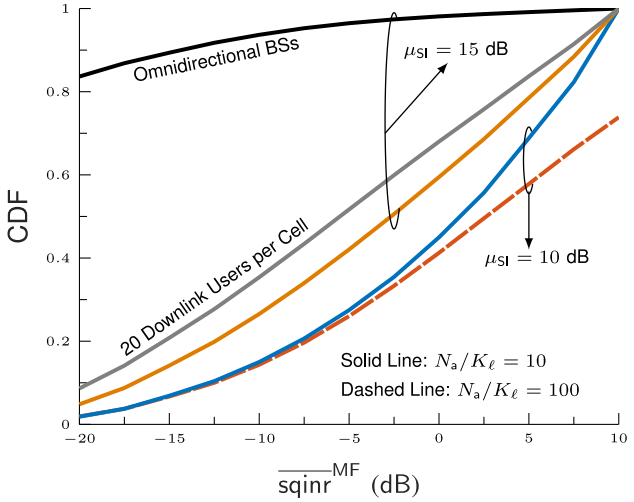

FIGURE 11. Reverse link results: Effects of antenna gain, SI channel power and number of downlink UEs on the CDF of the SQINR. Unless otherwise stated, the number of downlink UEs per cell is 10 users and the antenna array gain is 30 dB. The difference between red and blue curves is the value of the ratio N_{a}/K_ℓ. The difference between the gray and orange curves is the number of downlink users per cell, i.e., 20 vs. 10. The black curve is simulated using the default values except antenna gain is 0 dB.

This is confirmed when employing omnidirectional BSs, the CDF performance degrades, and vice versa.

Fig. 12 plots the effective spectral efficiency vs. number of ADC/DAC quantization bits (b). Spectral efficiency increases with b and converges to a ceiling defined by the full-resolution case. The rate decreases when adopting low-resolution ADC/DACs (i.e., having a small number of bits b). In addition, spectral efficiency noticeably degrades for 40W vs. 30W of SI power. Although FD is vulnerable to loop-back SI, FD outperforms HD mode which is one of the goals of this work. We evaluate a low mobility case (pedestrians) and a high mobility case (vehicles). Since the pedestrian

6. In this work, we define the notion of rate with outage as the average data rate that is correctly received/decoded at the receiver which is equivalent to the throughput. In other standards in the literature, the rate with outage is often synonymous with the transmit data rate. If we consider the rate with outage as the throughput, we would account for the probability of bursts (outage) by multiplying by the term $(1-\epsilon)$, while for the transmit data rate, the term $(1-\epsilon)$ would not be accounted for.

7. It is important to note here that these values for the parameters are selected from [32], [47], [62] subject to the standards to prove the validity of the obtained results. For all cases, 10^5 realizations of the random variables were generated to perform the Monte Carlo simulation in MATLAB.

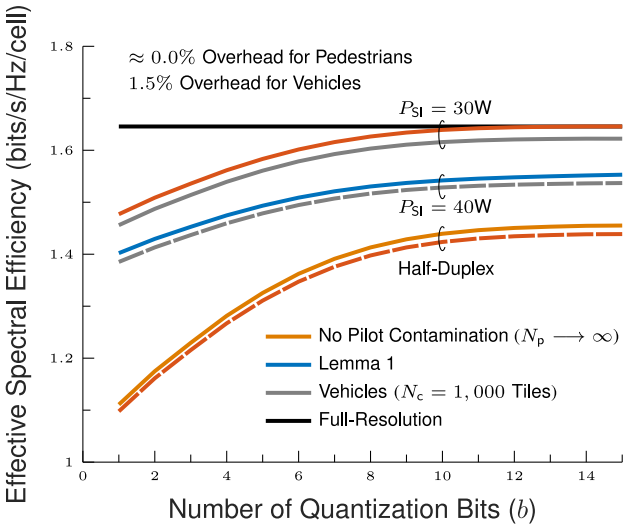

FIGURE 12. Reverse link results: Effects of SI power, overhead, ADC/DAC resolution, duplexing mode and pilot contamination on spectral efficiency. The dashed red curve is simulated for HD and accounts for pilot contamination unlike the solid yellow curve. The dashed gray curve is simulated using the default values in Table 4. A hexagonal grid is assumed for this simulation. The solid red curve is considered for pedestrians unlike the solid gray curve which is considered for vehicles.

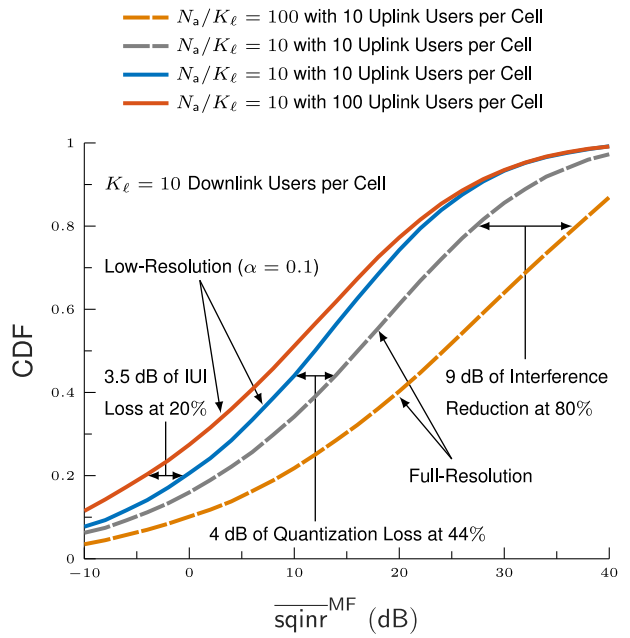

FIGURE 13. Forward link results: Effects of full-duplexing, ADC/DAC quantization error, and the ratio N_a/K_ℓ on the CDF of the SQINR. The dashed gray and solid blue curves are simulated for full and low resolution DAC, respectively.

model features a large fading coherence tile and hence low overhead, better effective spectral efficiency is achieved compared to the vehicular case that features a small fading coherence tile and hence higher overhead.

Fig. 13 plots the CDF, or outage probability, of the average forward link SQINR. When the number of reverse link users is large (e.g., 100 users per cell) and hence IUI is large, the CDF performance worsens, and vice versa. In addition, the performance improves with increasing ADC/DAC

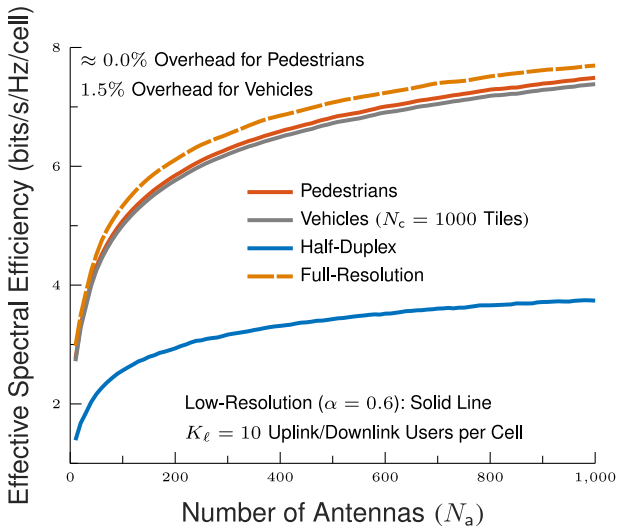

FIGURE 14. Forward link results: Effects of SI power, overhead, DAC resolution, duplexing mode and pilot contamination on the spectral efficiency. Dashed yellow curve stands for full-resolution, pedestrians and FD. Solid red and gray curves stand for low-resolution and FD. Solid blue curve stands for low-resolution DAC, HD and pedestrians scenario.

resolution. By significantly increasing the ratio N_a/K_ℓ, the user beams become exceedingly narrow, and the desired signal dominates the noise and interference. This factor, for example, rejects about 9 dB of interference at a CDF of 80%. Although the increase of this factor is important, the SINR is limited by the pilot contamination which is corroborated by (56).

Fig. 14 shows the forward link spectral efficiency vs. number of BS antennas for low and full DAC resolution. Since the pedestrian mobility features a large fading coherence tile and hence low overhead, better spectral efficiency is achieved vs. vehicular mobility that features a small fading coherence tile and hence higher overhead. In addition, we observe that the proposed system outperforms HD mode, which shows the feasibility of FD in cellular networks.

Fig. 15 plots the CDF, or outage probability, vs. forward link SQINR. In the CDF, the PPP tessellation exceeds the hexagonal lattice except for a small range of 5–8 dB of forward link SNR. In addition, the performance decreases with increasing inter-user interference incurred by FD operation of the BS and uplink UEs transmission. The plot shows the loss incurred by the low-resolution ADC/DAC is about 2 dB when the CDF saturates.

Fig. 16 plots the energy efficiency vs. number of quantization bits b for three ADC generations. Each generation shows the number of ADC bits that gives maximum energy efficiency, e.g., 8 bits for HPADC, 11 bits for IPADC and 15 bits for LPDAC described in Section VII-A, with energy efficiency increasing for b lower than this value and decreasing for b greater than this value. The optimal point is influenced by both the saturation of the spectral efficiency as b increases, which depends on SNR, and by the ADC power consumption model, which increases with b. Comparing

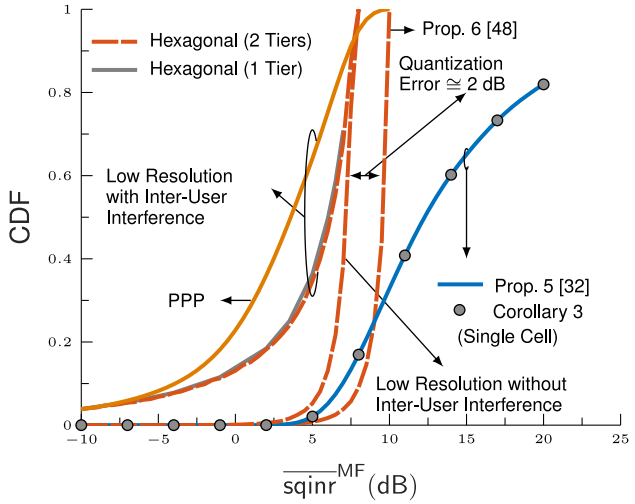

FIGURE 15. Forward link results: Effects of full-duplexing, quantization error, and network cell shapes on outage probability (CDF) with quantizer gains $\alpha_u = \alpha_d = 0.6$. The results are simulated without accounting for pilot contamination.

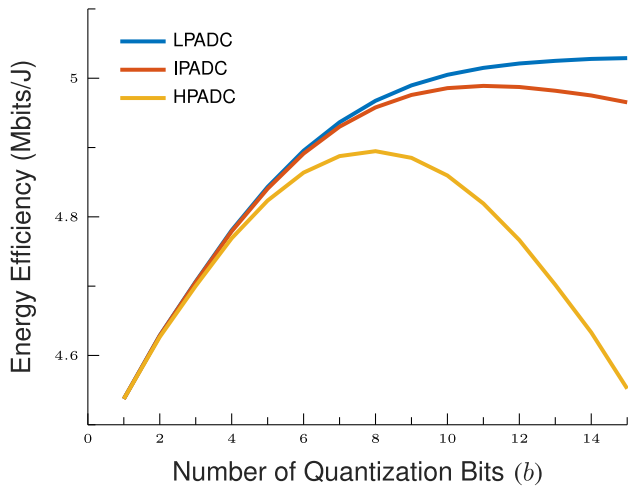

FIGURE 16. Reverse link results: Energy efficiency vs. number of quantization bits for three ADC generations using values of Walden's figure of merit c given in Table 6.

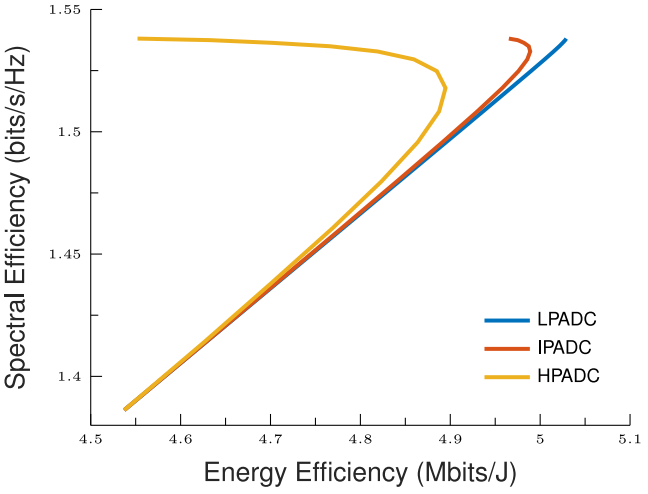

FIGURE 17. Reverse link results: Spectral efficiency vs. energy efficiency for three ADC generations using values of Walden's figure of merit c given in Table 6.

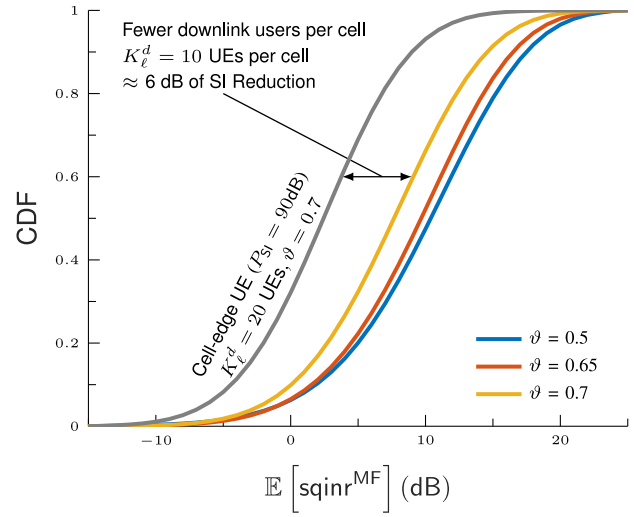

FIGURE 18. Large-scale distribution of $\mathbb{E}[\text{sqinr}^{\text{MF}}]$ based LMMSE estimation in the reverse link of a two-tier hexagonal network with fractional power control (ϑ) and SI power (P_{SI}). A cell-edge user is considered for the simulation with 3 bits of ADC resolution at the BS. The gray and yellow curves are simulated for the same power control ($\vartheta = 0.7$) but with a different number of downlink users per cell. The blue, red and yellow curves correspond to the same simulation parameters including the same number of downlink UEs = 10, but with different power control coefficients (ϑ).

ADC generations, the power consumption of the legacy LPADC model increases at a higher rate vs. b than for either IPADC or HPADC models.

Fig. 17 plots the spectral vs. energy efficiency for three ADC generations. In the chart, we notice curves that evolve as the number of bits b is increased, reaching upward and right up to a point where they wrap around themselves and energy efficiency returns to the top left corner. Each curve can be interpreted as an "operating region" where the BS receiver can be implemented. The more extended the area covered by a receiver, the more versatile the corresponding design; the closer a curve to the top-right corner, the better the corresponding architecture. We observe that the energy efficiency only increases up to a certain number of bits due to the fact that for a smaller number of bits b, the spectral efficiency increases more than the power, and the energy efficiency increases. However, for a larger number of bits b, the power consumption increases faster than the spectral efficiency, thereby resulting in a decrease of the energy efficiency while the spectral efficiency still increases. This occurs due to the fact that the power consumption of ADC increases exponentially, whereas the spectral efficiency increases sub-linearly, with an increase in the number of ADC bits.

Fig. 18 plots the CDF of the SQINR based on LMMSE channel estimation for different fractional power control values as well as SI power. The primary motivations for a fractional power control policy in the cellular reverse link are to provide beneficial coverage enhancements for the lowest-percentile users, who are typically at the cell-edge, and manage the average transmit power of battery-powered

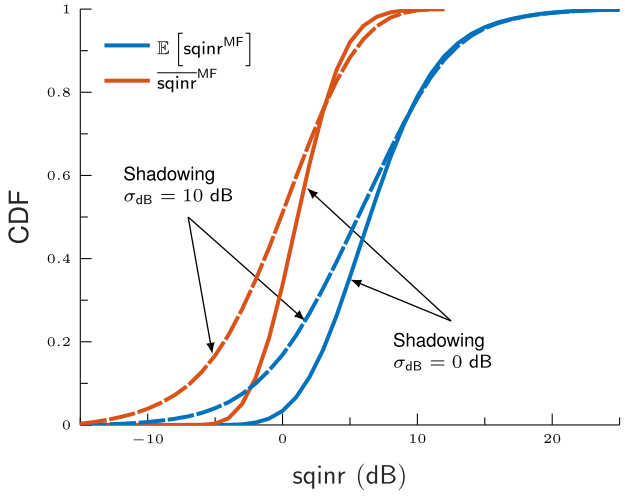

FIGURE 19. Large-scale distribution of $\mathbb{E}[\text{sqinr}^{\text{MF}}]$ based LMMSE estimation and $\overline{\text{sqinr}}^{\text{MF}}$ based channel hardening in the reverse link of a two-tier hexagonal network without power control. For ADC resolution, $b = 3$ bits is assumed.

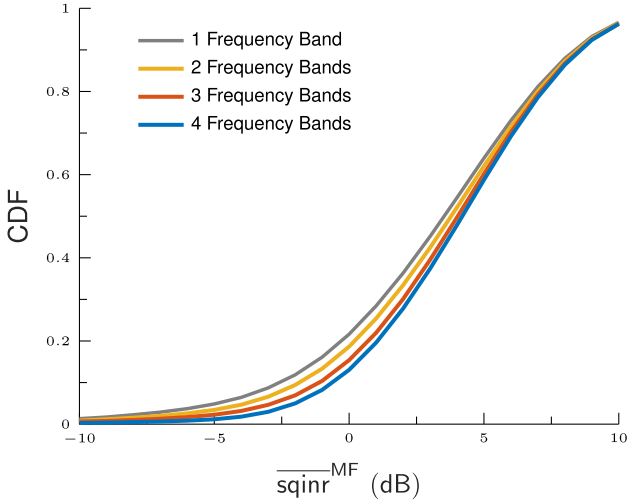

FIGURE 20. Large-scale CDF vs. $\overline{\text{sqinr}}^{\text{MF}}$ based channel hardening in the forward link for a PPP network for four different numbers of frequency bands, Δ. For ADC resolution, $b = 3$ bits is assumed.

UE devices. In practical cellular systems such as LTE and New Radio (NR), fractional power control policy is network-specific and not user-specific; thus, there needs to be some optimization carried out to select parameters that can provide acceptable performance for the majority of users and bestow a high overall system capacity. For $\vartheta = 0$, the fractional power control policy reverts to a fixed-power transmission. For $\vartheta > 0$, conversely, it compresses the dynamic range of the received power by a factor ϑ. At high SNR, the use of larger values ϑ affects the CDF since the users closest to their serving BSs greatly decrease their transmit power relative to the users at the cell-edge. Exponent values for ϑ in the range of 0.5 to 0.7 have been identified as providing a satisfactory balance between cell-edge and aggregate performance [57]. In addition, the cell-edge features high SI power of around 90 dB. When the number of forward link UEs decreases, the forward link transmit power at the BSs decreases resulting in lowering the SI power by approximately 6 dB and hence improving the CDF.

Fig. 19 plots the CDF of the large-scale distribution for LMMSE channel estimation and channel hardening as well as different values of the shadowing standard deviation. We observe that $\overline{\text{sqinr}}^{\text{MF}}$ (channel hardening) tracks $\mathbb{E}[\text{sqinr}^{\text{MF}}]$ (LMMSE channel estimation) most of the way with a gap of roughly 7 dB. Certainly, $\overline{\text{sqinr}}_k^{\text{MF}} \leq \mathbb{E}[\text{sqinr}_k^{\text{MF}}]$, $k = 0, \ldots, K-1$ because to evaluate $\overline{\text{sqinr}}_1^{\text{MF}}, \ldots, \overline{\text{sqinr}}_{K-1}^{\text{MF}}$, we have unconditioned on $\hat{\mathbf{h}}_0, \ldots, \hat{\mathbf{h}}_{K-1}$ and $\mathbf{w}_k$, thereby depriving the receiver of information. However, the performance of a channel hardening-based receiver is less complex to compute, and deep into the massive MIMO regime; it is hardly inferior but instead serves as a tight lower bound and convenient analytical tool. We further observe that the shadowing strength raises the lower tail of the SQINR distribution at the expense of a slight reduction in the upper tail of the CDF near saturation.

Cellular network service providers must guarantee a minimum Quality of Service (QoS) for their customers such as rate and coverage probability. Commercial cellular network designers must find a way to increase and maintain a satisfied coverage probability. For the case where the network is interference-limited, a robust way to improve the coverage is to decrease the number of interfering BSs. This can be carried out using fractional frequency reuse policy wherein $\Delta \geq 1$ is the reuse factor that determines the number of various frequency bands exploited by the network, where one band is used per cell. From the independent thinning Theorem of PPP [72, Theorem 2.36], it follows that the interfering BSs that transmit in the same frequency band are a thinned version of the original PPP and have a density $\lambda_{\text{BS}}/\Delta$. Note that the thinned version of a PPP is also a PPP. Increasing the frequency reuse factor leads to minimizing the interference and hence improving the outage probability (CDF) as shown by Fig. 20. When $\Delta \longrightarrow \infty$, cellular interference is completely eliminated and hence the network becomes noise-limited.

The desirable increase in coverage with increasing Δ has to be balanced against the fact that each cell can only exploit $1/\Delta$-th of the available frequencies. Fig. 21 shows the optimal fractional frequency reuse Δ from the average spectral efficiency perspective is in fact $\Delta = 1$; i.e., any increase in coverage from frequency reuse is paid for by decreasing the sum spectral efficiency in the network. Therefore, increasing the number of frequency bands can lead to non-efficient use of the spectrum and hence degrade the spectral efficiency. We also observe spectral efficiency improves with increasing pathloss. In fact, this is explained by the fact that since the network is interference-limited, the higher pathloss exponent would also reduce the power of the interfering signals, thereby leading to the spectral efficiency improvement.

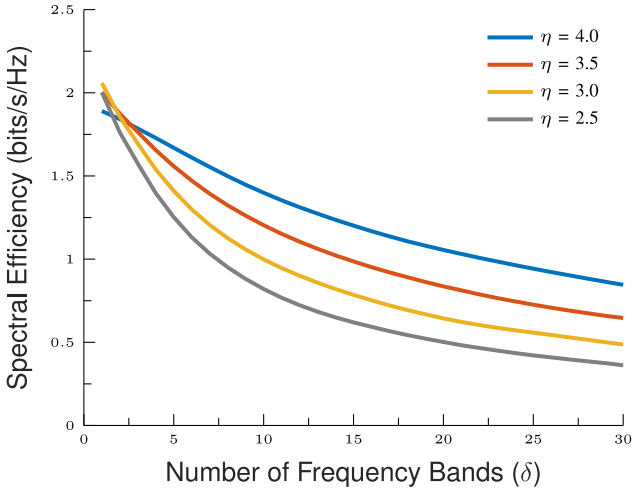

FIGURE 21. Spectral efficiency vs. number of frequency bands for the large-scale $\overline{\text{sqinr}}^{\text{MF}}$ based channel hardening in the reverse link for a PPP network. Simulations are considered for different values of the pathloss (η) as well as 3 bits of ADC resolution.

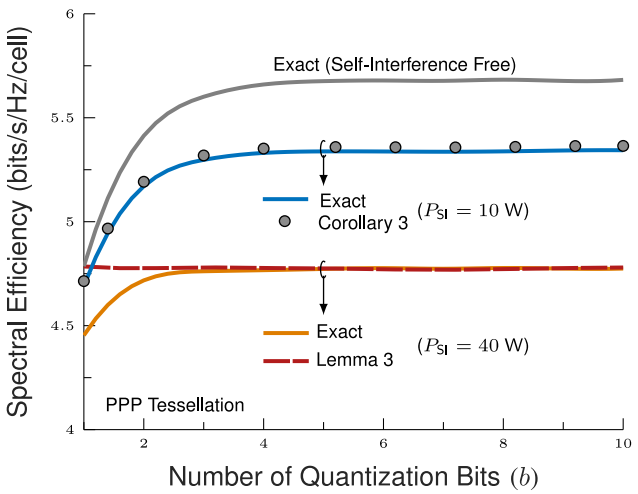

FIGURE 22. Spectral efficiency vs. number of quantization bits for large-scale distribution $\overline{\text{sqinr}}^{\text{MF}}$ in the reverse link for a PPP network. We assume $N_{\text{a}} = 1000$ antennas at the BS.

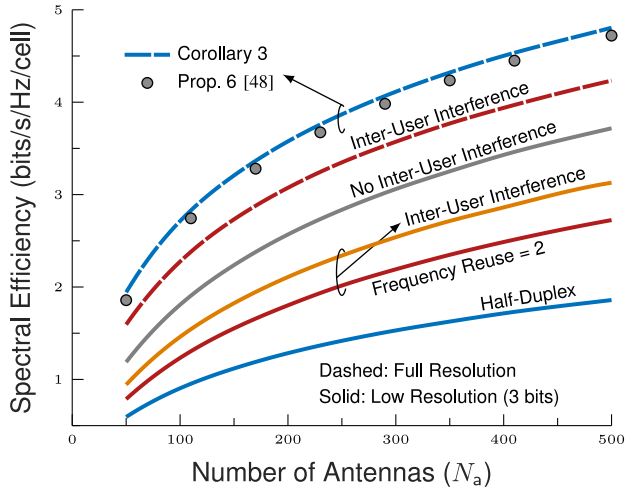

FIGURE 23. Spectral efficiency vs. number of antennas for large-scale distribution $\overline{\text{sqinr}}^{\text{MF}}$ in the forward link for a PPP network. The default value of frequency reuse factor is 1.

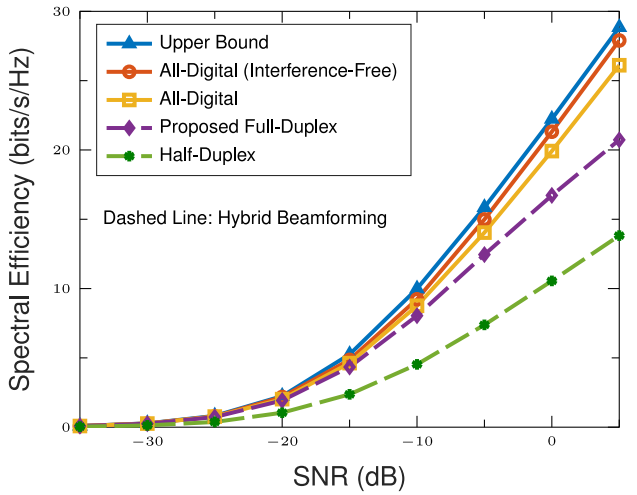

FIGURE 24. Reverse link spectral efficiency results for single cell, multiuser scenario: Comparison of the proposed FD hybrid beamforming algorithm with the HD case, all-digital beamforming, and upper bound. 5 users are uniformly dropped in the cell.

Fig. 22 simulates the reverse link spectral efficiency vs. number of quantization bits (b) for a PPP tessellation network. Spectral efficiency increases with b and converges to a ceiling derived by (62) in Lemma 3; the rate decreases when adopting low-resolution ADCs and DACs (low b). Spectral efficiency degrades for 10W and 40W of SI power vs. the SI-free case.

Fig. 23 shows the forward link spectral efficiency increasing with the number of quantization bits b and BS antennas for a PPP tessellation. When considering low and full resolution data converters, spectral efficiency converges to a fixed ceiling with enough antennas, which agrees with (69) in Lemma 6.

Fig. 24 illustrates the performance of the reverse link spectral efficiency vs. average SNR. We observe that the proposed hybrid beamforming FD design achieves better spectral efficiency than the HD mode, and the relative gap increases with average SNR. Moreover, there are losses in spectral efficiency between the proposed design in comparison with the benchmarks of the all-digital case (wherein an RF chain is dedicated to each antenna element) and the upper bound. These losses are incurred by the unit modulus constraint as well as the limited number of RF chains in the hybrid architecture which itself is a loss in the DoF.

Fig. 25 shows the performance of the forward link spectral efficiency vs. average SNR. We notice that the performance improves with the number of RF chains at the BS and approaches the all-digital performance with 8 RF chains. In fact, increasing the number of RF chains is equivalent to providing more DoF to cancel the interference and achieve a spatial multiplexing gain, thereby resulting in good spectral efficiency.

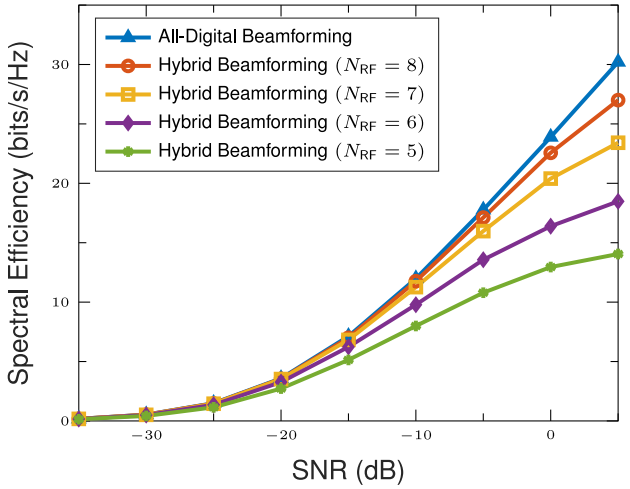

FIGURE 25. Forward link spectral efficiency results for single cell, multiuser scenario. Comparison between all-digital and hybrid beamforming for different numbers of RF chains at the BS. 5 users are uniformly placed in the cell.

IX. CONCLUSION

In this work, we provided a unified framework for full-duplex cellular networks with low resolution ADCs/DACs. Using the framework, we developed analytical expressions for the SQINR and spectral efficiency and for forward and reverse links under pilot contamination, LMMSE channel estimation and channel hardening. The proposed modeling accounts for pilot overhead, self-interference, and network geometry such as hexagonal lattice, square grid and PPP tessellation. Matched filter receivers and precoders are applied at the receive and transmit arrays of the BSs, respectively, to further reduce complexity.

Further, we derived special cases, asymptotic results and power scaling laws to unpack several engineering insights of the proposed model. First, if the number of antennas N_{a} and number of resolution bits b are held fixed and the power goes to infinity, the spectral efficiency for the reverse and forward links are saturated by a ceiling determined by the number of antennas and the ADC/DAC resolution gains. Second, if the power scales with the number of antennas and the latter becomes massive, cellular interference including pilot contamination, inter-cell interference, and intra-cell interference vanishes except for the SI power. Third, if the ratio of the number of antennas N_{a} and the number of users per cell K_ℓ goes to infinity, cellular interference is rejected but pilot contamination and SI power remain. We also observe spectral efficiency improves with increasing pathloss. In fact, this is explained by the fact that since the network is interference-limited, the higher pathloss exponent would also reduce the interfering signals power, thereby leading to the spectral efficiency improvement.

Furthermore, we extended the analysis of sub-7 GHz LTE bands to support mmWave bands. In the analysis, we introduced a signal processing perspective on hybrid analog/digital beamforming, a problem formulation of the hybrid beamforming design and benchmarking tools such as the impractical all-digital beamforming approach and an upper bound on the spectral efficiency.

We also analyzed power consumption and investigated the effects of ADC/DAC power, Walden's figure merit for ADCs/DACs, and the number of quantization bits on energy efficiency. In addition, the overall system performance is quantified in terms of effective spectral efficiency and outage probability (i.e., cumulative distribution function of the large-scale distribution of the SQINR). Using a proper scaling ratio of the number of antennas N_{a} over number of users per cell K_ℓ, a large amount of interference can be rejected as previously mentioned; this justifies the use of matched filter beamforming which is less complex than MMSE and ZF filters. Although the SQINR is limited by pilot contamination for a massive number of antennas, this effect is not pronounced.

Simulation results show the quantization error, SI, and IUI incur rate losses; however, the rate loss can be compensated by employing a large number of BS antennas as well as high resolution ADCs/DACs in the UEs. The hefty power consumption in the BSs due to having a large number of antennas can be reduced by employing low resolution ADCs/DACs. The simulation results also corroborated the robustness of the proposed FD mode compared to the HD mode, which is one of the goals of this work to demonstrate the feasibility of the FD in cellular networks.

Finally, analytical expressions derived for matched filters are widely applicable, as corroborated by a multitude of examples. This wide applicability of the proposed reverse and forward link analysis makes its extension to other low-complex and yet resilient transmit and receive strategies, power allocation, user association policies and even channel conditions, highly attractive.

APPENDIX A
PROOF OF THE LMMSE CHANNEL ESTIMATE

During channel estimation in the reverse link, the BSs switch to operate in HD mode and full-resolution so that the received signal at the BS of interest becomes

$$\mathbf{y}_k = \sqrt{G_k P_k}\mathbf{h}_k + \sum_{\ell\in\mathcal{C}} \sqrt{G_{\ell,k} P_{\ell,k}}\mathbf{h}_{\ell,k} + \mathbf{v}_k. \tag{86}$$

The LMMSE equalizer is

$$\mathbf{w}^{\mathsf{MMSE}} = \left(G_k P_k + \sum_{\ell\in\mathcal{C}} G_{\ell,k} P_{\ell,k} + \sigma^2 \right)^{-1} \sqrt{G_k P_k}\mathbf{I}. \tag{87}$$

Therefore, the LMMSE channel estimate ($\hat{\mathbf{h}}_k = \mathbf{w}^{\mathsf{MMSE}}\mathbf{y}_k$) is

$$\hat{\mathbf{h}}_k = \frac{G_k P_k}{G_k P_k + \sum_{\ell\in\mathcal{C}} G_{\ell,k} P_{\ell,k} + \sigma^2} \times \left(\mathbf{h}_k + \sum_{\ell,\in\mathcal{C}} \sqrt{\frac{G_{\ell,k} P_{\ell,k}}{G_k P_k}}\mathbf{k}_{\ell,k} + \frac{v_k}{\sqrt{G_k P_k}} \right). \tag{88}$$

By properly scaling the numerator and denominator by the noise power, we have

$$\hat{\mathbf{h}}_k = \frac{\frac{G_k P_k}{\sigma^2}}{\frac{G_k P_k + \sum_{\ell\in\mathcal{C}} G_{\ell,k} P_{\ell,k} + \sigma^2}{\sigma^2}} \times \left(\mathbf{h}_k + \sum_{\ell\in\mathcal{C}} \sqrt{\frac{\frac{G_{k,\ell} P_{\ell,k}}{G_k P_k}}{\sigma^2}} \mathbf{h}_{\ell,k} + \frac{\mathbf{v}_k}{\sqrt{G_k P_k}} \right), \quad (89)$$

which leads to the result in (19) with $\mathbf{v}'_k = \mathbf{v}_k/\sqrt{G_k P_k}$ and

$$\frac{1}{N_{\mathsf{a}}} \mathbb{E}\left[\|\mathbf{v}'_k\|^2 \right] = \frac{1}{N_{\mathsf{a}}} N_{\mathsf{a}} \frac{|\mathbf{v}_{k,i}|^2}{G_k P_k} = \frac{\sigma^2}{G_k P_k} = \frac{1}{\frac{P_k}{P_u}\mathsf{SNR}_k^u}. \quad (90)$$

The estimation error is $\tilde{\mathbf{h}}_k = \mathbf{h}_k - \hat{\mathbf{h}}_k$, which is

$$\begin{aligned} \tilde{\mathbf{h}}_k = & \frac{1 + \sum_{\ell\in\mathcal{C}} \frac{P_{\ell,k}}{P_u} \mathsf{SNR}_{\ell,k}^u}{1 + \frac{P_k}{P_u}\mathsf{SNR}_k^u + \sum_{\ell\in\mathcal{C}} \frac{P_{\ell,k}}{P_u}\mathsf{SNR}_{\ell,k}^u} \mathbf{h}_k \\ & - \frac{\frac{P_k}{P_u}\mathsf{SNR}_k^u}{1 + \frac{P_k}{P_u}\mathsf{SNR}_k^u + \sum_{\ell\in\mathcal{C}} \frac{P_{\ell,k}}{P_u}\mathsf{SNR}_{\ell,k}^u} \sum_{\ell\in\mathcal{C}} \sqrt{\frac{\frac{P_{\ell,k}\mathsf{SNR}_{\ell,k}^u}{P_u}}{\frac{P_k \mathsf{SNR}_k^u}{P_u}}} \mathbf{h}_{\ell,k} \\ & - \frac{\frac{P_k}{P_u}\mathsf{SNR}_k^u}{1 + \frac{P_k}{P_u}\mathsf{SNR}_k^u + \sum_{\ell\in\mathcal{C}} \frac{P_{\ell,k}}{P_u}\mathsf{SNR}_{\ell,k}^u} \mathbf{v}'_k. \end{aligned} \quad (91)$$

While the variance of the estimation error is calculated as

$$\mathsf{MMSE}_k = \frac{1 + \sum_{\ell\in\mathcal{C}} \frac{P_{\ell,k}}{P_u}\mathsf{SNR}_{\ell,k}^u}{1 + \frac{P_k}{P_u}\mathsf{SNR}_k^u + \sum_{\ell\in\mathcal{C}} \frac{P_{\ell,k}}{P_u}\mathsf{SNR}_{\ell,k}^u}. \quad (92)$$

APPENDIX B
PROOF OF THEOREM 1

The derivations of the terms related to SI and aggregate AQNM in the denominator of (23) are straightforward. We will focus on deriving the remaining terms.

The desired signal is the component projected onto what the receiver regards as the true channel for the k-th uplink user, $\hat{\mathbf{h}}_k$, while the projection onto the estimation error $\tilde{\mathbf{h}}_k$ is treated as additional Gaussian noise (filtered by $\mathbf{w}_k$). The inter-cell interference, included within the noise, is made explicit in this formulation, but also treated as Gaussian noise (filtered by $\mathbf{h}_k$). Conditioned on $\hat{\mathbf{h}}_0, \ldots, \hat{\mathbf{h}}_{K-1}$ and $\mathbf{w}_k$, which the BS of interest is privy to, the output SQINR for user k equals to (23) where we have capitalized on the independence between $\mathbf{w}_k$ and $\tilde{\mathbf{h}}_{\mathrm{k}}$, for $\mathrm{k} = 0, \ldots, K-1$, to develop

$$\begin{aligned} \mathbb{E}\left[\left| \mathbf{w}_k^* \mathbf{h}_{\mathrm{k}} \right|^2 | \mathbf{w}_k \right] &= \mathbb{E}\left[\mathbf{w}_k^* \tilde{\mathbf{h}}_{\mathrm{k}} \tilde{\mathbf{h}}_{\mathrm{k}}^* \mathbf{w}_k | \mathbf{w}_k \right] \\ &= \mathbf{w}_k^* \mathbb{E}\left[\tilde{\mathbf{h}}_{\mathrm{k}} \tilde{\mathbf{h}}_{\mathrm{k}}^* \right] \mathbf{w}_k \\ &= \mathbf{w}_k^* \left(\mathsf{MMSE}_{\mathrm{k}} \cdot \mathbf{I} \right) \mathbf{w}_k \\ &= \mathsf{MMSE}_{\mathrm{k}} \|\mathbf{w}_k\|^2. \end{aligned} \quad (93)$$

As far as the inter-cell interference goes, the term $\mathbb{E}[|\mathbf{h}_{\ell,\mathrm{k}}^* \mathbf{h}_{\ell,\mathrm{k}}|^2 | \mathbf{w}_k] = \mathbf{w}_k^* \mathbb{E}[\mathbf{h}_{\ell,\mathrm{k}} \mathbf{h}_{\ell,\mathrm{k}}^* | \mathbf{w}_k] \mathbf{w}_k$ cannot be further elaborated in complete generality for copilot interferers, i.e., for $\ell \in \mathcal{C}$ and $\mathrm{k} = k$, because $\mathbf{w}_k$ is contaminated by, and therefore it is not independent of, $\mathbf{h}_{\ell,k}$ whenever $\ell \in \mathcal{C}$. For noncopilot interferers, though, $\mathbf{w}_k$ and $\mathbf{h}_{\ell,\mathrm{k}}$ do exhibit independence and thus

$$\mathbf{w}_k^* \mathbb{E}\left[\mathbf{h}_{\ell,\mathrm{k}} \mathbf{h}_{\ell,\mathrm{k}}^* | \mathbf{w}_k \right] \mathbf{w}_k = \mathbf{w}_k^* \mathbb{E}\left[\mathbf{h}_{\ell,\mathrm{k}} \mathbf{h}_{\ell,\mathrm{k}}^* \right] \mathbf{w}_k = \|\mathbf{w}_k\|^2. \quad (94)$$

Therefore, we obtain the expression (23) in Theorem 1.

APPENDIX C
PROOF OF THEOREM 3

The derivation of the terms in (37) are straightforward except for the term $\mathbb{E}[\mathbf{h}_{\ell,k} \mathbf{h}_{\ell,k}^* | \mathbf{w}_k^{\mathsf{MF}}]$. For a matched filter receiver $\mathbf{w}_k^{\mathsf{MF}}$, using the results of Corollary 1 and after some mathematical manipulations, the conditional covariance of the copilot interference can be evaluated as

$$\begin{aligned} & \mathbb{E}\left[\mathbf{h}_{\ell,k} \mathbf{h}_{\ell,k}^* | \mathbf{w}_k^{\mathsf{MF}} \right] \\ & = \mathbf{I} + \frac{\frac{P_{\ell,k}}{P_u}\mathsf{SNR}_{\ell,k}^u}{1 + \frac{P_k}{P_u}\mathsf{SNR}_k^u + \sum_{l\in\mathcal{C}} \frac{P_{k,l}}{P_u}\mathsf{SNR}_{l,k}^u} \left(\mathbf{w}_k^{\mathsf{MF}} \mathbf{w}_k^{\mathsf{MF}*} - \mathbf{I} \right). \end{aligned} \quad (95)$$

After substituting (95) in (36), we prove the results of Theorem 3.

APPENDIX D
PROOF OF THEOREM 4

From the expression of the SQINR (38), $\overline{\mathsf{den}}_u^{\mathsf{MF}}$ can be written as (96). Using Corollary 2, we derive the terms of (96) as

$$\mathsf{var}\left[\left| \mathbf{w}_k^{\mathsf{MF}*} \mathbf{h}_k \right|^2 \right] = \mathbb{E}\left[\left| \mathbf{w}_k^{\mathsf{MF}*} \mathbf{h}_k \right|^2 \right]$$

$$\begin{aligned} \overline{\mathsf{den}}_u^{\mathsf{MF}} = & \alpha_u^2 \frac{P_k}{P_u} \mathsf{SNR}_k^u \mathsf{var}\left[\mathbf{w}_k^{\mathsf{MF}*} \mathbf{h}_k \right] + \alpha_u^2 \sum_{\mathrm{k}\neq k} \frac{P_{\mathrm{k}}}{P_u} \mathsf{SNR}_{\mathrm{k}}^u \mathbb{E}\left[\left| \mathbf{w}_k^{\mathsf{MF}*} \mathbf{h}_{\mathrm{k}} \right|^2 \right] + \alpha_u^2 \sum_{\ell\in\mathcal{C}} \frac{P_{\ell,k}}{P_u} \mathsf{SNR}_{\ell,k}^u \mathbb{E}\left[\left| \mathbf{w}_k^{\mathsf{MF}*} \mathbf{h}_{\ell,k} \right|^2 \right] \\ & + \alpha_u^2 N_{\mathsf{a}} \left(1 + \sum_{\substack{\ell\neq 0 \\ \ell\notin\mathcal{C}}} \sum_{\mathrm{k}=0}^{K_\ell^u - 1} \frac{P_{\ell,\mathrm{k}}}{P_u} \mathsf{SNR}_{\ell,\mathrm{k}}^u + \sum_{\ell\in\mathcal{C}} \sum_{\mathrm{k}\neq k} \frac{P_{\ell,\mathrm{k}}}{P_u} \mathsf{SNR}_{\ell,\mathrm{k}}^u \right) + \frac{\alpha_u^2}{\sigma^2} P_{\mathsf{SI}} \mathbb{E}\left[\left| \mathbf{w}_k^{\mathsf{MF}*} \mathbf{H}_{\mathsf{SI}} \mathbf{q}_d \right|^2 \right] \\ & + \frac{\alpha_d^2 \alpha_u^2}{\sigma^2} P_{\mathsf{SI}} \sum_{\mathrm{k}=0}^{K-1} \mathbb{E}\left[\left| \mathbf{w}_k^{\mathsf{MF}*} \mathbf{H}_{\mathsf{SI}} \mathbf{f}_{\mathrm{k}} \right|^2 \right] + \frac{1}{\sigma^2} \mathbb{E}\left[\left| \mathbf{w}_k^{\mathsf{MF}*} \mathbf{q}_u^2 \right| \right] \end{aligned} \quad (96)$$

$$\frac{1}{\sigma^2}\mathbb{E}\left[\left|\mathbf{w}_k^{\mathsf{MF}*}\mathbf{q}_u\right|^2\right] = N_{\mathsf{a}}\alpha_u(1-\alpha_u)\left[2\frac{P_k}{P_u}\mathsf{SNR}_k^u + \sum_{\mathrm{k}\neq k}\frac{P_{\mathrm{k}}}{P_u}\mathsf{SNR}_{\mathrm{k}}^u + \sum_{\ell\neq 0}\sum_{\mathrm{k}}\frac{P_{\ell,\mathrm{k}}}{P_u}\mathsf{SNR}_{\ell,\mathrm{k}}^u + \alpha_d N_{\mathsf{a}}\mathsf{INR} + 1\right] \tag{102}$$

$$\begin{aligned}\overline{\mathsf{den}}_d^{\mathsf{MF}} &= \alpha_d^2\frac{P_k}{P_d N_{\mathsf{a}}}\mathsf{SNR}_k^d\mathsf{var}\left[\mathbf{h}_k^*\mathbf{f}_k^{\mathsf{MF}}\right] + \alpha_d^2\sum_{\mathrm{k}\neq k}\frac{P_{\mathrm{k}}}{P_d N_{\mathsf{a}}}\mathsf{SNR}_k^d\mathbb{E}\left[\left|\mathbf{h}_k^*\mathbf{f}_{\mathrm{k}}^{\mathsf{MF}}\right|^2\right] + \alpha_d^2\sum_{\ell\in\mathcal{C}}\frac{P_{\ell,k}}{P_d N_{\mathsf{a}}}\mathsf{SNR}_{\ell,k}^d\mathbb{E}\left[\left|\mathbf{h}_{\ell,k}^*\mathbf{f}_{\ell,k}^{\mathsf{MF}}\right|^2\right]\\ &+ \alpha_d^2\sum_{\substack{\ell\neq 0\\ \ell\notin\mathcal{C}}}\sum_{\mathrm{k}=0}^{K_\ell^u-1}\frac{P_{\ell,\mathrm{k}}}{P_d N_{\mathsf{a}}}\mathsf{SNR}_{\ell,k}^d\mathbb{E}\left[\left|\mathbf{h}_{\ell,k}^*\mathbf{f}_{\ell,\mathrm{k}}^{\mathsf{MF}}\right|^2\right] + \alpha_d^2\sum_{\ell\in\mathcal{C}}\sum_{\mathrm{k}\neq k}\frac{P_{\ell,\mathrm{k}}}{P_d N_{\mathsf{a}}}\mathsf{SNR}_{\ell,\mathrm{k}}^d\mathbb{E}\left[\left|\mathbf{h}_{\ell,k}^*\mathbf{f}_{\ell,\mathrm{k}}^{\mathsf{MF}}\right|^2\right]\\ &+ \sum_{\ell}\sum_{\mathrm{k}=0}^{K_\ell^u-1}\frac{P_{\ell,\mathrm{k}}^u}{P_u}\mathsf{SNR}_{(\ell,\mathrm{k}),k}^{\mathsf{iui}}\mathbb{E}\left[\left|\mathbf{g}_{(\ell,\mathrm{k}),k}\right|^2\right] + \sum_{\ell}\frac{P_{\ell,k}^d}{P_d N_{\mathsf{a}}}\mathsf{SNR}_{\ell,k}^d\mathbb{E}\left[\left|\mathbf{h}_{\ell,k}^*\mathbf{q}_{d,\ell}\right|^2\right] + 1\end{aligned} \tag{103}$$

$$\begin{aligned}\overline{\mathsf{den}}_d^{\mathsf{MF}} &= 1 + \alpha_d^2\sum_{\ell}\mathsf{SNR}_{\ell,k}^d + \alpha_d^2 N_{\mathsf{a}}\sum_{\ell\in\mathcal{C}}\frac{\frac{P_k}{P_u}\mathsf{SNR}_{\ell,k}^u}{1+\frac{P_k}{P_u}\mathsf{SNR}_{\ell,k}^u + \sum_{l\in\mathcal{C}}\frac{P_{l,k}}{P_u}\mathsf{SNR}_{\ell,(l,k)}^u}\frac{P_{\ell,k}}{P_d}\mathsf{SNR}_{\ell,k}^d\\ &+ \sum_{\ell}\sum_{\mathrm{k}=0}^{K_\ell^u-1}\frac{P_{\ell,\mathrm{k}}^u}{P_u}\mathsf{SNR}_{(\ell,\mathrm{k}),k}^{\mathsf{iui}} + \alpha_d(1-\alpha_d)\sum_{\ell}\frac{P_{\ell,k}}{P_d}\mathsf{SNR}_{\ell,k}^d\left(K_\ell^d+1\right)\end{aligned} \tag{105}$$

$$\begin{aligned}&- \frac{\frac{P_k}{P_u}\mathsf{SNR}_k^u}{1+\frac{P_k}{P_u}\mathsf{SNR}_k^u + \sum_{\ell\in\mathcal{C}}\frac{P_{\ell,k}}{P_u}\mathsf{SNR}_{\ell,k}^u}N_{\mathsf{a}}^2\\ &= N_{\mathsf{a}}.\end{aligned} \tag{97}$$

Since $\mathbf{w}_k^{\mathsf{MF}}$ and $\mathbf{h}_{\mathrm{k}}$ are independent for $\mathrm{k}\neq k$

$$\begin{aligned}\mathbb{E}\left[\left|\mathbf{w}_k^{\mathsf{MF}*}\mathbf{h}_{\mathrm{k}}\right|^2\right] &= \mathbb{E}\left[\mathbf{w}_k^{\mathsf{MF}*}\overbrace{\mathbb{E}\left[\mathbf{h}_{\mathrm{k}}\mathbf{h}_{\mathrm{k}}^*\right]}^{\mathbf{I}}\mathbf{w}_k^{\mathsf{MF}}\right]\\ &= \mathbb{E}\left[\left\|\mathbf{w}_k^{\mathsf{MF}}\right\|^2\right]\\ &= N_{\mathsf{a}}.\end{aligned} \tag{98}$$

The unconditional copilot interference power equals to

$$\begin{aligned}&\mathbb{E}\left[\left|\mathbf{w}_k^{\mathsf{MF}*}\mathbf{h}_{\ell,k}\right|^2\right]\\ &= N_{\mathsf{a}} + \frac{\frac{P_{\ell,k}}{P_u}\mathsf{SNR}_{\ell,k}^u}{1+\frac{P_k}{P_u}\mathsf{SNR}_k^u + \sum_{l\in\mathcal{C}}\frac{P_{l,k}}{P_u}\mathsf{SNR}_{\ell,k}^u}N_{\mathsf{a}}^2.\end{aligned} \tag{99}$$

Since $\mathbf{w}_k^{\mathsf{MF}}$, $\mathbf{H}_{\mathsf{SI}}$ and $\mathbf{q}_d$ are mutually independent

$$\begin{aligned}\mathbb{E}\left[\left|\mathbf{w}_k^{\mathsf{MF}*}\mathbf{H}_{\mathsf{SI}}\mathbf{q}_d\right|^2\right] &= \mathbb{E}\left[\mathbf{w}_k^{\mathsf{MF}*}\mathbb{E}\left[\mathbf{H}_{\mathsf{SI}}\mathbf{H}_{\mathsf{SI}}^*\right]\left[\mathbf{q}_d\mathbf{q}_d^*\right]\mathbf{w}_k^{\mathsf{MF}}\right]\\ &= \alpha_d(1-\alpha_d)K^d\mu_{\mathsf{SI}}^2 N_{\mathsf{a}}^2\end{aligned} \tag{100}$$

In addition, the mutual independence of $\mathbf{w}_k^{\mathsf{MF}}$, $\mathbf{H}_{\mathsf{SI}}$ and $\mathbf{f}_{\mathrm{k}}^{\mathsf{MF}}$ yields

$$\sum_{\mathrm{k}=0}^{K^d-1}\mathbb{E}\left[\left|\mathbf{w}_k^{\mathsf{MF}*}\mathbf{H}_{\mathsf{SI}}\mathbf{f}_{\mathrm{k}}^{\mathsf{MF}}\right|^2\right] = \mu_{\mathsf{SI}}^2 K^d N_{\mathsf{a}}^2. \tag{101}$$

Using [32, Appendix A], the last term of (96) is given by (102), shown at the top of the page, where $\mathsf{INR} = P_{\mathsf{SI}}\mu_{\mathsf{SI}}^2/\sigma^2$. The derivation of the above terms leads to the results of Theorem 4.

APPENDIX E
PROOF OF THEOREM 6

In Theorem 6, initially the denominator $\overline{\mathsf{den}}_d^{\mathsf{MF}}$ of the output SQINR is expressed by (103), shown at the top of the page. Using [32, Appendix A], the 7-th term of (103) can be simplified as follows:

$$\begin{aligned}&\sum_{\ell}\frac{P_{\ell,k}}{P_d N_{\mathsf{a}}}\mathsf{SNR}_{\ell,k}^d\mathbb{E}\left[\left|\mathbf{h}_{\ell,k}^*\mathbf{q}_{d,\ell}\right|^2\right]\\ &= \alpha_d(1-\alpha_d)\sum_{\ell}\frac{P_{\ell,k}}{P_d}\mathsf{SNR}_{\ell,k}^d\left(K_\ell^d+1\right).\end{aligned} \tag{104}$$

The first 5 terms of (103) can be derived using results from the reverse link analysis (97)-(99) as well as Corollary 2. After mathematical manipulations, (103) can be simplified as (105), shown at the top of the page. While introducing the new term $\varrho = \mathsf{SNR}_{\ell,(l,k)}^d/\mathsf{SNR}_{\ell,(l,k)}^u$ for any ℓ, l and k as the *forward-reverse SNR ratio*, (105) can be reduced to (55) and hence Theorem 6 is proved.

REFERENCES

[1] E. Balti and B. L. Evans, "Reverse link analysis for full-duplex cellular networks with low resolution ADC/DAC," in *Proc. IEEE Int. Workshop Signal Process. Adv. Wireless Commun.*, 2022, pp. 1–5.
[2] E. Balti and B. L. Evans, "Forward link analysis for full-duplex cellular networks with low resolution ADC/DAC," in *Proc. IEEE Int. Workshop Signal Process. Adv. Wireless Commun.*, 2022, pp. 1–5.

[3] E. Balti and B. L. Evans, "Full-duplex massive MIMO cellular networks with low resolution ADC/DAC," in *Proc. IEEE Global Commun. Conf. Wireless Commun. (Globecom WC)*, Rio de Janeiro, Brazil, Dec. 2022.

[4] O. Tipmongkolsilp, S. Zaghloul, and A. Jukan, "The evolution of cellular backhaul technologies: Current issues and future trends," *IEEE Commun. Surveys Tuts.*, vol. 13, no. 1, pp. 97–113, 1st Quart., 2011.

[5] S. H. R. Naqvi and P.-H. Ho, "Achieving 5G NR mmWave indoor coverage under integrated access backhaul," *IEEE Syst. J.*, vol. 15, no. 4, pp. 5429–5439, Dec. 2021.

[6] M. Gapeyenko, V. Petrov, D. Moltchanov, S. Andreev, N. Himayat, and Y. Koucheryavy, "Flexible and reliable UAV-assisted backhaul operation in 5G mmWave cellular networks," *IEEE J. Sel. Areas Commun.*, vol. 36, no. 11, pp. 2486–2496, Nov. 2018.

[7] N. Kouzayha, H. Elsawy, H. Dahrouj, K. Alshaikh, T. Y. Al-Naffouri, and M.-S. Alouini, "Analysis of large scale aerial terrestrial networks with mmWave backhauling," *IEEE Trans. Wireless Commun.*, vol. 20, no. 12, pp. 8362–8380, Dec. 2021.

[8] I. P. Roberts, J. G. Andrews, and S. Vishwanath, "Hybrid beamforming for millimeter wave full-duplex under limited receive dynamic range," *IEEE Trans. Wireless Commun.*, vol. 20, no. 12, pp. 7758–7772, Dec. 2021.

[9] I. P. Roberts, J. G. Andrews, H. B. Jain, and S. Vishwanath, "Millimeter-wave full duplex radios: New challenges and techniques," *IEEE Wireless Commun.*, vol. 28, no. 1, pp. 36–43, Feb. 2021.

[10] P. Anokye, R. K. Ahiadormey, H.-S. Jo, C. Song, and K.-J. Lee, "Low-resolution ADC quantized full-duplex massive MIMO-enabled wireless backhaul in heterogeneous networks over Rician channels," *IEEE Trans. Wireless Commun.*, vol. 19, no. 8, pp. 5503–5517, Aug. 2020.

[11] E. Balti and B. L. Evans, "Hybrid beamforming design for wideband mmWave full-duplex systems," 2021, *arXiv:2107.06166*.

[12] E. Balti and N. Mensi, "Zero-forcing max-power beamforming for hybrid mmWave full-duplex MIMO systems," in *Proc. Int. Conf. Adv. Syst. Emergent Technol.*, 2020, pp. 344–349.

[13] E. Balti and B. L. Evans, "Joint beamforming and interference cancellation in mmWave wideband full-duplex systems," 2021, *arXiv:2110.12266*.

[14] "The 5G evolution: 3GPP releases 16–17." 2020. [Online]. Available: https://www.5gamericas.org/wp-content/uploads/2020/01/5G-Evolution-3GPP-R16-R17-FINAL.pdf

[15] A. Koc and T. Le-Ngoc, "Full-duplex mmWave massive MIMO systems: A joint hybrid precoding/combining and self-interference cancellation design," *IEEE Open J. Commun. Soc.*, vol. 2, pp. 754–774, 2021.

[16] J. Zhang, N. Garg, M. Holm, and T. Ratnarajah, "Design of full duplex millimeter-wave integrated access and backhaul networks," *IEEE Wireless Commun.*, vol. 28, no. 1, pp. 60–67, Feb. 2021.

[17] K. E. Kolodziej, J. P. Doane, B. T. Perry, and J. S. Herd, "Adaptive beamforming for multi-function in-band full-duplex applications," *IEEE Wireless Commun.*, vol. 28, no. 1, pp. 28–35, Feb. 2021.

[18] T. Chen, M. B. Dastjerdi, H. Krishnaswamy, and G. Zussman, "Wideband full-duplex phased array with joint transmit and receive beamforming: Optimization and rate gains," *IEEE/ACM Trans. Netw.*, vol. 29, no. 4, pp. 1591–1604, Aug. 2021.

[19] C. K. Sheemar, C. K. Thomas, and D. Slock, "Practical hybrid beamforming for millimeter wave massive MIMO full duplex with limited dynamic range," *IEEE Open J. Commun. Soc.*, vol. 3, pp. 127–143, 2022.

[20] D. W. Bliss, P. A. Parker, and A. R. Margetts, "Simultaneous transmission and reception for improved wireless network performance," in *Proc. IEEE Workshop Stat. Signal Process.*, 2007, pp. 478–482.

[21] T. Riihonen, S. Werner, and R. Wichman, "Mitigation of loopback self-interference in full-duplex MIMO relays," *IEEE Trans. Signal Process.*, vol. 59, no. 12, pp. 5983–5993, Dec. 2011.

[22] T. Riihonen, S. Werner, and R. Wichman, "Spatial loop interference suppression in full-duplex MIMO relays," in *Proc. Asilomar Conf. Signals Syst. Comput.*, 2009, pp. 1508–1512.

[23] B. D. Antwi-Boasiako, R. K. Ahiadormey, P. Anokye, and K.-J. Lee, "On the performance of massive MIMO full-duplex relaying with low-resolution ADCs," *IEEE Commun. Lett.*, vol. 26, no. 6, pp. 1259–1263, Jun. 2022.

[24] K. Xu, Z. Shen, Y. Wang, X. Xia, and D. Zhang, "Hybrid time-switching and power splitting SWIPT for full-duplex massive MIMO systems: A beam-domain approach," *IEEE Trans. Veh. Technol.*, vol. 67, no. 8, pp. 7257–7274, Aug. 2018.

[25] P. Zhu, Z. Sheng, J. Bao, and J. Li, "Antenna selection for full-duplex distributed massive MIMO via the elite preservation genetic algorithm," *IEEE Commun. Lett.*, vol. 26, no. 4, pp. 922–926, Apr. 2022.

[26] H. Q. Ngo, H. A. Suraweera, M. Matthaiou, and E. G. Larsson, "Multipair full-duplex relaying with massive arrays and linear processing," *IEEE J. Sel. Areas Commun.*, vol. 32, no. 9, pp. 1721–1737, Sep. 2014.

[27] S. Wang, Y. Liu, W. Zhang, and H. Zhang, "Achievable rates of full-duplex massive MIMO relay systems over Rician fading channels," *IEEE Trans. Veh. Technol.*, vol. 66, no. 11, pp. 9825–9837, Nov. 2017.

[28] A. Shojaeifard, K.-K. Wong, M. Di Renzo, G. Zheng, K. A. Hamdi, and J. Tang, "Massive MIMO-enabled full-duplex cellular networks," *IEEE Trans. Commun.*, vol. 65, no. 11, pp. 4734–4750, Nov. 2017.

[29] J. Zhang, L. Dai, Z. He, S. Jin, and X. Li, "Performance analysis of mixed-ADC massive MIMO systems over Rician fading channels," *IEEE J. Sel. Areas Commun.*, vol. 35, no. 6, pp. 1327–1338, Jun. 2017.

[30] P. Anokye, R. K. Ahiadormey, and K.-J. Lee, "Full-duplex cell-free massive MIMO with low-resolution ADCs," *IEEE Trans. Veh. Technol.*, vol. 70, no. 11, pp. 12179–12184, Nov. 2021.

[31] B. Murmann. "ADC performance survey 1997–2016." 2016. [Online]. Available: http://web.stanford.edu/ñurmann/adcsurvey.html

[32] J. Dai, J. Liu, J. Wang, J. Zhao, C. Cheng, and J.-Y. Wang, "Achievable rates for full-duplex massive MIMO systems with low-resolution ADCs/DACs," *IEEE Access*, vol. 7, pp. 24343–24353, 2019.

[33] Q. Ding, Y. Lian, and Y. Jing, "Performance analysis of full-duplex massive MIMO systems with low-resolution ADCs/DACs over Rician fading channels," *IEEE Trans. Veh. Technol.*, vol. 69, no. 7, pp. 7389–7403, Jul. 2020.

[34] J. Zhang, L. Dai, Z. He, B. Ai, and O. A. Dobre, "Mixed-ADC/DAC multipair massive MIMO relaying systems: Performance analysis and power optimization," *IEEE Trans. Commun.*, vol. 67, no. 1, pp. 140–153, Jan. 2019.

[35] T. Liu, J. Tong, Q. Guo, J. Xi, Y. Yu, and Z. Xiao, "Energy efficiency of massive MIMO systems with low-resolution ADCs and successive interference cancellation," *IEEE Trans. Wireless Commun.*, vol. 18, no. 8, pp. 3987–4002, Aug. 2019.

[36] A. Mezghani, J. A. Nossek, and A. L. Swindlehurst, "Low SNR asymptotic rates of vector channels with one-bit outputs," *IEEE Trans. Inf. Theory*, vol. 66, no. 12, pp. 7615–7634, Dec. 2020.

[37] T. Liu, J. Tong, Q. Guo, J. Xi, Y. Yu, and Z. Xiao, "On the performance of massive MIMO systems with low-resolution ADCs and MRC receivers over Rician fading channels," *IEEE Syst. J.*, vol. 15, no. 3, pp. 4514–4524, Sep. 2021.

[38] C. Kong, C. Zhong, S. Jin, S. Yang, H. Lin, and Z. Zhang, "Full-duplex massive MIMO relaying systems with low-resolution ADCs," *IEEE Trans. Wireless Commun.*, vol. 16, no. 8, pp. 5033–5047, Aug. 2017.

[39] N. Liang and W. Zhang, "Mixed-ADC massive MIMO," *IEEE J. Sel. Areas Commun.*, vol. 34, no. 4, pp. 983–997, Apr. 2016.

[40] J. Zhang, L. Dai, S. Sun, and Z. Wang, "On the spectral efficiency of massive MIMO systems with low-resolution ADCs," *IEEE Commun. Lett.*, vol. 20, no. 5, pp. 842–845, May 2016.

[41] T. L. Marzetta, "Noncooperative cellular wireless with unlimited numbers of base station antennas," *IEEE Trans. Wireless Commun.*, vol. 9, no. 11, pp. 3590–3600, Nov. 2010.

[42] A. D. Wyner, "Shannon-theoretic approach to a Gaussian cellular multiple-access channel," *IEEE Trans. Inf. Theory*, vol. 40, no. 6, pp. 1713–1727, Nov. 1994.

[43] J. Xu, J. Zhang, and J. G. Andrews, "On the accuracy of the Wyner model in cellular networks," *IEEE Trans. Wireless Commun.*, vol. 10, no. 9, pp. 3098–3109, Sep. 2011.

[44] J. G. Andrews, F. Baccelli, and R. K. Ganti, "A tractable approach to coverage and rate in cellular networks," *IEEE Trans. Commun.*, vol. 59, no. 11, pp. 3122–3134, Nov. 2011.

[45] T. D. Novlan, H. S. Dhillon, and J. G. Andrews, "Analytical modeling of uplink cellular networks," *IEEE Trans. Wireless Commun.*, vol. 12, no. 6, pp. 2669–2679, Jun. 2013.

[46] D. B. Taylor, H. S. Dhillon, T. D. Novlan, and J. G. Andrews, "Pairwise interaction processes for modeling cellular network topology," in *Proc. IEEE Global Commun. Conf.*, Dec. 2012, pp. 4524–4529.
[47] G. George, A. Lozano, and M. Haenggi, "Massive MIMO forward link analysis for cellular networks," *IEEE Trans. Wireless Commun.*, vol. 18, no. 6, pp. 2964–2976, Jun. 2019.
[48] H. ElSawy, A. Sultan-Salem, M.-S. Alouini, and M. Z. Win, "Modeling and analysis of cellular networks using stochastic geometry: A tutorial," *IEEE Commun. Surveys Tuts.*, vol. 19, no. 1, pp. 167–203, 1st Quart., 2017.
[49] B. Błaszczyszyn, M. Haenggi, P. Keeler, and S. Mukherjee, *Stochastic Geometry Analysis of Cellular Networks*. Cambridge, U.K.: Cambridge Univ. Press, 2018.
[50] W.-T. Li, Y.-C. Chiang, J.-H. Tsai, H.-Y. Yang, J.-H. Cheng, and T.-W. Huang, "60-GHz 5-bit phase shifter with integrated VGA phase-error compensation," *IEEE Trans. Microw. Theory Techn.*, vol. 61, no. 3, pp. 1224–1235, Mar. 2013.
[51] M. R. Akdeniz et al., "Millimeter wave channel modeling and cellular capacity evaluation," *IEEE J. Sel. Areas Commun.*, vol. 32, no. 6, pp. 1164–1179, Jun. 2014.
[52] X. Yu, J. Dai, and J. Shi, "Achievable rates of full-duplex massive MIMO systems with mixed-ADC/DAC," in *Proc. IEEE 21st Int. Conf. High Perform. Comput. Commun. IEEE 17th Int. Conf. Smart City IEEE 5th Int. Conf. Data Sci. Syst. (HPCC/SmartCity/DSS)*, 2019, pp. 1692–1698.
[53] O. Orhan, E. Erkip, and S. Rangan, "Low power analog-to-digital conversion in millimeter wave systems: Impact of resolution and bandwidth on performance," in *Proc. Inf. Theory Appl. Workshop*, 2015, pp. 191–198.
[54] L. Fan, S. Jin, C.-K. Wen, and H. Zhang, "Uplink achievable rate for massive MIMO systems with low-resolution ADC," *IEEE Commun. Lett.*, vol. 19, no. 12, pp. 2186–2189, Dec. 2015.
[55] X. Zhang, T. Liang, K. An, G. Zheng, and S. Chatzinotas, "Secure transmission in cell-free massive MIMO with RF impairments and low-resolution ADCs/DACs," *IEEE Trans. Veh. Technol.*, vol. 70, no. 9, pp. 8937–8949, Sep. 2021.
[56] S. Almonacil, F. Boitier, and P. Layec, "Performance model and design rules for optical systems employing low-resolution DAC/ADC," *J. Lightw. Technol.*, vol. 38, no. 11, pp. 3007–3014, Jun. 1, 2020.
[57] R. W. Heath Jr. and A. Lozano, *Foundations of MIMO Communication*. Cambridge, U.K.: Cambridge Univ. Press, 2018.
[58] Y. Cho, J. Choi, and B. L. Evans, "Coordinated beamforming in quantized massive MIMO systems with per-antenna constraints," in *Proc. IEEE Wireless Commun. Netw. Conf.*, Apr. 2022, pp. 2512–2517.
[59] E. Bjornson, M. Matthaiou, and M. Debbah, "A new look at dual-hop relaying: Performance limits with hardware impairments," *IEEE Trans. Commun.*, vol. 61, no. 11, pp. 4512–4525, Nov. 2013.
[60] X. Yu, J.-C. Shen, J. Zhang, and K. B. Letaief, "Alternating minimization algorithms for hybrid precoding in millimeter wave MIMO systems," *IEEE J. Sel. Topics Signal Process.*, vol. 10, no. 3, pp. 485–500, Apr. 2016.
[61] P.-A. Absil, R. Mahony, and R. Sepulchre, *Optimization Algorithms on Matrix Manifolds*. Princeton, NJ, USA: Princeton Univ. Press, 2009.
[62] T. D. Novlan and J. G. Andrews, "Analytical evaluation of uplink fractional frequency reuse," *IEEE Trans. Commun.*, vol. 61, no. 5, pp. 2098–2108, May 2013.
[63] W. B. Abbas, F. Gomez-Cuba, and M. Zorzi, "Millimeter wave receiver efficiency: A comprehensive comparison of beamforming schemes with low resolution ADCs," *IEEE Trans. Wireless Commun.*, vol. 16, no. 12, pp. 8131–8146, Dec. 2017.
[64] Y. Yu, P. G. M. Baltus, A. de Graauw, E. van der Heijden, C. S. Vaucher, and A. H. M. van Roermund, "A 60 GHz phase shifter integrated with LNA and PA in 65 nm CMOS for phased array systems," *IEEE J. Solid-State Circuits*, vol. 45, no. 9, pp. 1697–1709, Sep. 2010.
[65] L. Kong, "Energy-efficient 60 GHz phased-array design for multi-Gb/s communication systems," Ph.D. dissertation, Dept. Electr. Eng. Comput. Sci., Univ. California, Berkeley, CA, USA, Dec. 2014. [Online]. Available: http://www2.eecs.berkeley.edu/Pubs/TechRpts/2014/EECS-2014-191.html
[66] Y.-H. Lin and H. Wang, "A low phase and gain error passive phase shifter in 90 nm CMOS for 60 GHz phase array system application," in *IEEE MTT-S Int. Microw. Symp. Dig.*, 2016, pp. 1–4.
[67] M. Kraemer, D. Dragomirescu, and R. Plana, "Design of a very low-power, low-cost 60 GHz receiver front-end implemented in 65 nm CMOS technology," *Int. J. Microw. Wireless Technol.*, vol. 3, no. 2, pp. 131–138, 2011.
[68] R. Méndez-Rial, C. Rusu, N. González-Prelcic, A. Alkhateeb, and R. W. Heath, "Hybrid MIMO architectures for millimeter wave communications: Phase shifters or switches?" *IEEE Access*, vol. 4, pp. 247–267, 2016.
[69] B. Nasri, S. P. Sebastian, K.-D. You, R. RanjithKumar, and D. Shahrjerdi, "A 700 μW 1GS/s 4-bit folding-flash ADC in 65nm CMOS for wideband wireless communications," in *Proc. IEEE Int. Symp. Circuits Sys.*, 2017, pp. 1–4.
[70] W. B. Abbas, F. Gomez-Cuba, and M. Zorzi, "mmWave receiver beamforming comparison tool v1.0." Accessed: Mar. 20, 2021. [Online]. Available: http://enigma.det.uvigo.es/fgomez/mmWaveADCwebviewer/
[71] A. Lozano and N. Jindal, "Transmit diversity vs. spatial multiplexing in modern MIMO systems," *IEEE Trans. Wireless Commun.*, vol. 9, no. 1, pp. 186–197, Jan. 2010.
[72] M. Haenggi, *Stochastic Geometry for Wireless Networks*. Cambridge, U.K.: Cambridge Univ. Press, 2012.

ELYES BALTI (Graduate Student Member, IEEE) received the B.S. degree in electrical engineering from the École Supérieure des Communications de Tunis, Tunisia, in 2013, and the M.S. degree in electrical engineering from the University of Idaho, Moscow, ID, USA, in 2018. He is currently pursuing the Ph.D. degree in electrical engineering with The University of Texas at Austin, Austin, TX, USA, where he is a member of the Wireless Networking and Communications Group and 6G@UT Research Center. He has held summer internships with Motorola Mobility, Chicago, IL USA, in 2019; Huawei, Bridgewater, NJ, USA, in 2020; and Qualcomm, San Diego, CA, USA in 2021 and 2022, respectively. His research interests are in wireless communications, signal processing, and massive MIMO.

BRIAN L. EVANS (Fellow, IEEE) received the double major degree in electrical engineering and computer science from the Rose-Hulman Institute of Technology in 1987, and the M.S. and Ph.D. degrees in electrical engineering from the Georgia Institute of Technology in 1988 and 1993, respectively. From 1993 to 1996, he was a Postdoctoral Researcher with the University of California at Berkeley. In 1996, he joined the Faculty with The University of Texas at Austin, where he is currently an Engineering Foundation Professor with the Department of Electrical and computer Engineering. He has published more than 280 refereed journal articles and conference papers, and graduated 31 Ph.D. and 13 M.S. students. His research and teaching interests are in signal processing and machine learning to increase connection speeds and reliability in wireless communication systems. His research group develops algorithms with implementation constraints in mind, and translates algorithms into design methods and embedded prototypes. He has received the three IEEE Best/Top Conference Paper Awards and five Teaching Awards. He was the UT Austin Faculty Senate President from 2019 to 2020, and received the 2021 UT Austin Presidential Civitatis Award for "recognition of dedicated and meritorious service to the university above and beyond the regular expectations of teaching, research and service." He received the 1997 U.S. National Science Foundation CAREER Award.